

1 **Evaluation of the NAQFC Driven by the NOAA Global Forecast**
2 **System Version 16: Comparison with the WRF-CMAQ ~~Downscaling~~**
3 **~~Method~~ During the Summer 2019 FIREX-AQ Campaign**

4 Youhua Tang^{1,2}, Patrick C. Campbell^{1,2}, Pius Lee¹, Rick Saylor¹, Fanglin Yang³, Barry Baker¹,
5 Daniel Tong^{1,2}, Ariel Stein¹, Jianping Huang^{3,4}, Ho-Chun Huang^{3,4}, Li Pan^{3,4}, Jeff McQueen³,
6 Ivanka Stajner³, Jose Tirado-Delgado^{5,6}, Youngsun Jung⁵, Melissa Yang⁷, Ilann Bourgeois^{8,9},
7 Jeff Peischl^{8,9}, Tom Ryerson⁹, Donald Blake¹⁰, Joshua Schwarz⁹,
8 Jose-Luis Jimenez⁸, James Crawford¹¹, Glenn Diskin⁷, Richard Moore⁷, Johnathan Hair⁷, Greg
9 Huey¹¹, Andrew Rollins⁹, Jack Dibb¹², Xiaoyang Zhang¹³

10 1. NOAA Air Resources Laboratory, College Park, MD, USA.

11 2. Center for Spatial Information Science and Systems, George Mason University, Fairfax, VA,
12 USA.

13 3. NOAA National Centers for Environmental Prediction, College Park, MD, USA

14 4. I.M. Systems Group Inc., Rockville, MD, USA

15 5. Office of Science and Technology Integration, NOAA National Weather Service, Silver
16 Spring, MD, USA

17 6. Eastern Research Group Inc, USA

18 7. NASA Langley Research Center, Hampton, VA, USA

19 8. Cooperative Institute for Research in Environmental Sciences, University of Colorado
20 Boulder, Boulder, CO, USA

21 9. NOAA Chemical Sciences Laboratory, Boulder, CO, USA

22 10. Department of Chemistry, University of California at Irvine, Irvine, CA, USA

23 11. School of Earth and Atmospheric Sciences, Georgia Institute of Technology, Atlanta, GA,
24 USA

25 12. Earth Systems Research Center, University of New Hampshire, Durham, NH, USA

26 13. Department of Geography & Geospatial Sciences, South Dakota State
27 University, Brookings, SD, USA

28
29 **Correspondence:** Youhua Tang (youhua.tang@noaa.gov)

30 **Abstract**

31 The latest operational National Air Quality Forecasting Capability (NAQFC) has been advanced
32 to use the Community Multi-scale Air Quality (CMAQ) model version 5.3.1 with CB6 (carbon
33 bond version 6)-Aero7 (version 7 of the aerosol module) chemical mechanism and is driven by
34 the Finite Volume Cubed-Sphere (FV3)-Global Forecast System, version 16 (GFSv16). This has
35 been accomplished by development of the meteorological preprocessor, NOAA-EPA
36 Atmosphere-Chemistry Coupler (NACC), which is adapted from the existing Meteorology-
37 Chemistry Interface Processor (MCIP). Differing from the typically used Weather Research and
38 Forecasting (WRF)/CMAQ system in the air quality research community, the interpolation-based
39 NACC can use various meteorological output to drive CMAQ (e.g., FV3-GFSv16) even though

1 they are in different grids. Here we compare and evaluate GFSv16-CMAQ vs. WRFv4.0.3-
2 CMAQ using observations over the contiguous United States (CONUS) in summer 2019. During
3 this period, the Fire Influence on Regional to Global Environments and Air Quality (FIREX-AQ)
4 field campaign was performed and we compare the two models with airborne measurements
5 mainly from the NASA DC-8 aircraft. The GFS-CMAQ and WRF-CMAQ systems have overall
6 similar performance with some differences for certain events, species and regions. The GFSv16
7 meteorology tends to have stronger planetary boundary layer height diurnal variability (higher
8 during daytime, and lower at night) than WRF over the U.S. Pacific coast, and it also predicted
9 lower nighttime 10-m winds. In summer 2019, GFS-CMAQ system showed better surface O₃
10 than WRF-CMAQ at night over the CONUS domain; however, their PM_{2.5} predictions showed
11 mixed verification results: GFS-CMAQ yielded better mean bias but poorer correlations over the
12 Pacific coast. These results indicate that using global GFSv16 meteorology with NACC to
13 directly drive CMAQ via the interpolation is feasible and yields reasonable results compared to
14 the commonly-used WRF ~~downscaling~~ driving approach.

16 1. Introduction

17 Traditionally, mesoscale meteorological models such as the Weather Research and Forecasting
18 Model (WRF) (Powers et al., 2017) are used as the meteorological drivers for air quality models
19 (AQMs) on the same ("native") model grid, such as Community Multiscale Air Quality Model
20 (CMAQ) (Byun & Schere, 2006). The NOAA National Weather Service's (NWS) National Air
21 Quality Forecasting Capability (NAQFC) has historically used a different approach, in which the
22 hourly meteorological outputs from prior operational models, such as North American Mesoscale
23 Model (NAM), need to be interpolated to the AQM grid to drive its air quality prediction. Prior
24 to this work, a "PREMAQ" coupler (Otte et al, 2004) combined both meteorological processing
25 and Sparse Matrix Operator Kernel Emissions (SMOKE) (Houyoux et al., 2000) processes, such
26 as point source plume rise effects. However, since the release of CMAQ version 5, the
27 meteorology-dependent plume rise, sea salt, and dust emission processes are included as inline
28 modules in CMAQ, and thus the corresponding emission processes are no longer needed in
29 PREMAQ. Furthermore, PREMAQ has no built-in interpolator, and thus relied on external
30 interpolators to remap the non-native-grid meteorological inputs, such as NAM, to the targeted
31 CMAQ domain, though it did perform vertical layer collapsing/interpolation to reduce layers.
32 The interpolation approach allows for more flexibility in using different meteorological drivers
33 (i.e., besides just WRF) for CMAQ; however, there is potential to raise mass-consistency issues
34 between models. It should be noted that the mass-consistency issues may also exist using native-
35 grid couplers (Byun, 1999a, 1999b), which can stem from the mass-inconsistent meteorological
36 inputs or due to the temporal interpolation of the input data. The well-developed offline AQMs,
37 such as CMAQ, have already considered such mass-consistency treatments using different
38 meteorological inputs (Byun et al., 1999c).

39
40 To upgrade the NAQFC system with the latest CMAQ chemistry and NOAA operational
41 meteorology, we developed an updated interpolation-based meteorological coupler, the NOAA-
42 EPA Atmosphere-Chemistry Coupler (NACC) (Campbell et al., 2022) adapted from the U.S.

1 EPA’s Meteorology-Chemistry Interface Processor (MCIP) version 5 (Otte and Pleim, 2010;
2 <https://github.com/USEPA/CMAQ>). The NACC system replaced PREMAQ, and effectively
3 couples the Finite-Volume Cubed-Sphere (FV3) Dynamical Core - Global Forecast System
4 version 16 (GFSv16) (Yang et al., 2020; Harris et al, 2021) to CMAQ v5.3.1 (hereafter referred
5 to as GFS-CMAQ). Campbell et al. (2022) described the development and application of the
6 GFS-CMAQ system using NACC (in their work referred to as “NACC-CMAQ”) and a
7 comprehensive comparison between the current (GFS-CMAQ since July 20, 2021) and previous
8 (NAM-CMAQv5.0.2) operational NAQFC model performances.
9

10 In this study, we analyze the impacts of the meteorological model drivers, and compare GFS-
11 CMAQ using NACC interpolation to the commonly-used ~~downscaled~~-native-grid WRF-CMAQ
12 application and its impact on air quality predictions. Yu et al. (2012a, 2012b) had previously
13 compared the CMAQ performance driven by WRF-NMM and WRF-ARW during the 2006
14 TexAQs/GoMACCS field campaign, and found that the NMM-CMAQ and ARW-CMAQ
15 showed overall similar performance with some differences for certain events, chemical species,
16 and regions. Similarly, this study focuses on the comparison of GFS-CMAQ versus WRF-
17 CMAQ (see Section 2, Methodology), and verifies the model performance against the aircraft
18 observations from the Fire Influence on Regional to Global Environments and Air Quality
19 (FIREX-AQ) field experiment during summer 2019 (Section 3). Surface verification is also
20 performed using AIRNow data for August 2019 (Section 4), serving as a benchmark for the new
21 NAQFC versus the traditional WRF-CMAQ used in the air quality modeling community.
22

23 **2. Methodology**

24 Here we compare the two CMAQ (version 5.3.1) runs driven by the interpolated GFSv16
25 meteorology (GFS-CMAQ) and WRF ~~downscaled~~-meteorology (WRF-CMAQ). All other
26 settings, such as emission and lateral boundary conditions are the same. The meteorology-
27 related physics is discussed in the following sections to address the models’ performance
28 discrepancies. Both the GFS-CMAQ and WRF-CMAQ simulations are run from a period
29 covering 12 July – 31 August, 2019, each using the last 10 days in July as the model spin-ups
30 that are not included in the analyses.
31

32 **2.1 GFS Meteorological Inputs**

33 The GFSv16 is the current operational global forecast system in NOAA/NCEP using FV3
34 dynamical core. Its detailed configuration can be found in Campbell et al. (2022) and Yang et al.
35 (2020). Compared to the previous version (v15), GFSv16 updated many physical schemes (Table
36 1) and added the parameterization for subgrid scale nonstationary gravity-wave drag. To use the
37 GFS’s meteorology to drive CMAQ, a meteorological coupler, NACC, is developed (Campbell
38 et al., 2022). Differing from the original MCIP which was developed to process WRF/ARW
39 meteorology for CMAQ, the NACC coupler interpolates non-native-grid meteorology to a user-

1 defined grid and has parallel processing capability, which drastically reduces its run time for
2 operational forecasts (Campbell et al., 2022). Currently, NACC's horizontal interpolation
3 employs two methods: bilinear and nearest-neighbor. In this study, we use the nearest-neighbor
4 method to categorical (discontinuous) variables that include land use types, vegetation fraction,
5 terrain elevation, Monin–Obukhov length, friction velocity, and soil temperatures, while the
6 bilinear interpolation is used for mainly smoothly varying (continuous) meteorological variables
7 that include wind fields, temperature, pressure, and specific humidity. The CMAQ model is
8 defined in the Arakawa C-grid (Arakawa and Lamb, 1977), and thus the GFSv16 horizontal wind
9 components (U, V) need to be interpolated to the perpendicular cell faces instead of the cell
10 center (Otte and Pleim, 2010) after rotation to the defined map projection. The scalar variables
11 are defined in the target grid cell center, and thus their ~~GFSv16~~ interpolations are more
12 straightforward: from GFSv16 A-grid to CMAQ A-grid. The NACC coupler can either use the
13 native layers or collapse (i.e., interpolate) to a set number of user-defined vertical layers for
14 CMAQ use. The GFSv16 has 127 vertical layers with global coverage in 13 km horizontal
15 resolution, where the targeted domain is a 12×12 km Contiguous United States (CONUS) with
16 35 vertical layers (Campbell et al, 2022). Here we use 24-hour GFSv16 forecasts starting at 12
17 UTC each day.

18
19 Most variables needed by CMAQ are directly interpolated from the GFSv16 outputs. The NACC
20 processor has options to calculate diagnostic variables, such as planetary boundary layer (PBL)
21 height, if they are needed. In this study, we use the interpolated GFSv16's PBL height instead of
22 the diagnostic one. It also has an option to import the externally provided land-surface variables.
23 Here we import updated 2018–2020 climatological averaged leaf area index (LAI) and NOAA
24 near-real-time (NRT) greenness vegetation fraction (GVF) from satellite-based Visible Infrared
25 Imaging Radiometer Suite (VIIRS) retrievals (Campbell et al., 2022). The updated satellite-based
26 LAI and GVF impact CMAQ's biogenic emissions and dry deposition processes, which were
27 described in detail in Campbell et al. (2022).

29 **2.2 WRF Meteorology**

30 To compare with GFSv16 meteorology processed by NACC, a corresponding WRF version 4.0.3
31 (Skamarock et al, 2021) simulation is run covering the NAQFC's native grid, which is a 12 km
32 horizontal resolution, Lambert conformal map projection over CONUS. Table 1 shows the WRF
33 configuration, which is commonly employed in CONUS meteorological and air quality studies in
34 the community, versus the current NOAA/NWS operational version of GFSv16. In contrast to
35 GFSv16, which is a global model that uses the NOAA/NCEP's Global Data Assimilation System
36 (GDAS) (https://www.emc.ncep.noaa.gov/data_assimilation/data.html) for its initial conditions
37 and runs on its own global dynamics and physics without any other constraints, the regional
38 WRF simulation uses ~~downscaled~~ GFSv16 for its initial conditions. In this study, GFSv16 was
39 re-initialized with GDAS every 24 hours, and WRF conducted the continuous run after spin-up.
40 Furthermore, WRF also ~~uses downscaled~~ takes its lateral boundary conditions ~~taken~~ from

1 GFSv16 every 6 hours. ~~Here For the WRF runs, continuously after spin-up and~~ we have enabled
2 the four-dimensional data assimilation (FDDA) for the u- and v-component winds, temperature,
3 and humidity (Table 1) every 6 hours, thus nudging towards GFSv16. This nudging method used
4 in WRF runs can help reduce the difference of two meteorological models, though its effect may
5 vary depending on events as WRF and GFS use different physics.

6
7 WRF and GFSv16 have similar settings for the land surface model, surface layer and radiation
8 schemes; however, their microphysics and PBL schemes are different (Table 1). Compared to the
9 35-layer WRF with a 100 hPa domain top, GFSv16 has a much higher domain top (0.2 hPa) and
10 127 vertical layers, which are collapsed by NACC to 35 sigma layers up to 14 km for CMAQ.
11 We use NACC (inherited from MCIP version 5.0) to process WRF hourly meteorology, while
12 maintaining the vertical layer structure. Thus, in contrast to GFS-CMAQ, the WRF-CMAQ
13 system uses the native grid without interpolation.

14 15 **2.3 CMAQ Configuration**

16 Here CMAQ version 5.3.1 (Appel et al., 2021) is used with the Carbon Bond 6 version r3
17 (CB6r3; Yarwood et al., 2010, 2014; Luecken, et al., 2019) chemical mechanism and Aero7
18 treatment of secondary organic aerosols (CB6r3_AE7_AQ). CMAQ 5.3.1 includes a series of
19 scientific updates from the previous version (Appel et al., 2021), including the updated air-
20 surface exchange and deposition modules, which showed significant impact on ozone prediction
21 compared to the previous NAQFC (Campbell et al., 2022). We also include the bi-directional
22 NH₃ (BIDI-NH₃) exchange model for NH₃ surface fluxes. An updated Biogenic Emissions
23 Landuse Dataset v5 (BELD5) is used in this study to drive the inline Biogenic Emissions
24 Inventory System (BEIS) version 3.61. The anthropogenic emissions are provided by the
25 National Emissions Inventory Collaborative (NEIC) with base year 2016 version 1 (NEIC
26 ~~2019~~2016). We replace the U.S. EPA default CMAQ dust emissions model with a ~~novel~~ inline
27 windblown dust model known as “FENGSHA” (Fu et al., 2014; Huang et al., 2015; Dong et al.,
28 2016). The FENGSHA dust scheme uses the sediment supply map and magnitude of the friction
29 velocity (USTAR) compared to a threshold friction velocity (UTHR) to calculate the potential of
30 dust emission flux. The UTHR depends on the land cover, soil type (clay fraction), and soil
31 moisture Campbell et al. (2022) ~~include the details of the CMAQ 5.3.1 configuration for this~~
32 ~~study.~~

33
34 We have updated the wildfire emissions system in CMAQv5.3.1 based on the Blended Global
35 Biomass Burning Emissions Product (GBBEPx) (Zhang and Kondragunta, 2006; Zhang et al.,
36 2011). The GBBEPx uses satellite-detected fire radiative power (FRP) to estimate wildfire
37 smoke emissions for a number of species: CO (carbon monoxide), NO_x (nitrogen oxides), SO₂
38 (sulfur dioxide), elemental carbon, ~~total~~ primarily emitted organic aerosols, and PM_{2.5}. The
39 satellite FRP is estimated from satellite brightness temperature anomaly, and the GBBEPx
40 processor assumes that the wildfire emissions are proportional to the FRP over certain land use

1 type in certain regions. The GBBEPx emissions are based on polar orbiting satellites: MODIS
2 (Aqua and Terra satellites) and VIIRS (Suomi-NPP and NOAA-20 satellites) instruments, which
3 are updated once per day. A wildfire emission preprocessor converts the GBBEPx emissions to
4 CMAQ-ready input files using emission speciation and diurnal profiles (high during daytime and
5 low at night) (adopted from U.S. EPA-based profiles) (Baker et al., 2016), and a daily scaling
6 factor. Here we classify the wildfire into either a long-lasting fire (longer than 24 hours) or short-
7 term fire (shorter than 24 hours) based on land use types and regions. As historic statistics shows
8 that most fires (>95%) in east of 110°W last less than 24 hours. Only-only the fires west of
9 110°W that have a model grid cell total forest fraction > 0.4 are assumed to be long-lasting fires;
10 which incur daily scaling factors of 1, 0.25, 0.25 for days 1, 2 and 3, respectively. All other
11 short-term GBBEPx fires are assumed to have smoke emissions for 24 hours (i.e., day 1 only).
12 Burning area could be highly uncertain as GBBEPx data do not have this information. One grid
13 cell could have multiply fires and some big fire could appear in several grids. Here we carry the
14 previous NAQFC's method, and apply a constant ratio: 10% of the grid cell, as the burning area
15 (Pan et al., 2020) according to Rolph et al (2009). CMAQ treats wildfire emissions as point
16 sources that undergo inline plume rise to distribute the smoke vertically. The default CMAQ
17 plume rise used here is based on Briggs (1965), which is driven by fire heat flux (converted from
18 FRP with a ratio of 1) and fixed burning area (assumed to be 10% of the 0.1°×0.1° grid cell).
19

20 3. Model Evaluations over the U.S. for August 2019

21 To first gain a general picture and compare the overall GFS-CMAQ and WRF-CMAQ model
22 performances, in this section we evaluate near-surface meteorological and air quality predictions
23 during the FIREX-AQ August 2019 period against NOAA's METEOROLOGICAL Aerodrome Report
24 (METAR; https://madis.ncep.noaa.gov/madis_metar.shtml) and the U.S. EPA's AirNow
25 (<https://www.airnow.gov/>) observation networks. -All the comparisons of meteorological
26 variables are for those actually used in CMAQ. For GFS-CMAQ, it refers to the interpolated
27 GFS data. Campbell et al (2022) included the detailed comparisons before and after
28 interpolation, showing that the interpolated meteorology was very consistent with the original
29 one. In this study, the model results are spatiotemporally interpolated to the corresponding
30 observation locations for comparison.
31

32 3.1 Domain-Wide Meteorology against the METAR Network

33 Figure 1 shows the mean bias (MB) of interpolated GFS and WRF predicted surface
34 meteorological variables compared to METAR data during August, 2019. Both meteorological
35 models have a cool bias over the Western and Northeastern United States, and a warm bias over
36 the western Rocky Mountain region and Southeastern United States (Figure 1a, 1b). Similar
37 temperature predictions are expected since WRF uses the FDDA method nudging toward GFS
38 data. However, GFS tends to be cooler than WRF over the Rocky Mountains and in the central
39 and northeastern USA due to their different dynamics and physics. The GFSv16 cold bias in the

1 lower troposphere is impacted by excessive evaporative cooling from rainfall (personal
2 communication with NOAA/NCEP). Campbell et al. (2022) had detailed discussions about
3 GFSv16 biases.

4
5 Both GFSv16 and WRF models have similar and rather significant dry biases for specific
6 humidity (SH) predictions across CONUS (Figure 1c, 1d). Qian et al (2020) investigated this
7 common dry bias in many models, and found that neglecting an irrigation contribution could
8 cause this dry bias. GFS has widespread dry biases (Campbell et al. 2022) and WRF has similar
9 dry biases, too as it is nudged toward GFS. There are some noticeable differences for certain
10 regions. For instance, WRF has less dry bias over Southern Texas than GFS.

11
12 Both models underestimate the mean 10-m wind speeds compared to METAR stations over the
13 western U.S. WRF has stronger underpredictions over the Rocky Mountains and overpredictions
14 over northeastern U.S., while GFS has stronger underpredictions over the Appalachian
15 Mountains and overpredictions over Texas and Oklahoma. GFSv16's operational verification
16 also (https://www.emc.ncep.noaa.gov/gmb/emc.glopara/vsdb/v16rt2/g2o/g2o_00Z/index.html)
17 shows that it tends to underpredict the 10-m wind over the western U.S. during both daytime and
18 nighttime, but shows overprediction over the eastern U.S. Besides the difference of physical
19 schemes, etc. (Table 1), other possible reasons causing this surface wind difference could be
20 effect of the gravity-wave drag (GFSv16 includes it, but the WRF run here does not), and
21 vertical resolution ~~(GFS's 127 layers versus WRF's 35 layers)~~, though they have similar
22 vertical layers below 1km (Campbell et al, 2022). Some studies (Skamarock et al, 2019) revealed
23 the necessity of fine vertical resolution for atmospheric simulations, especially within the PBL,
24 near tropospheric top, and during convective events. Insufficient vertical resolution could also
25 cause plume dilution on chemical transport modeling (Zhuang et al., 2018). The gravity-wave
26 drag is also known to ~~produce-influence synoptic-the synoptic-scale body forces dynamics~~ on the
27 atmospheric flow over irregularities at the earth's surface such as mountains and valleys, and
28 uneven distribution of diabatic heat sources associated with convective systems (Kim et al.,
29 2003). Its parameterization is needed for large-scale models.

30
31 There is strong regional variability in the monthly mean PBL height differences between GFS
32 and WRF during normal daytime (represented by 18 UTC) and nighttime (represented by 06
33 UTC) (Figure 2). During daytime, GFS has a higher PBL height compared to WRF over the U.S.
34 Pacific coast, northern Rocky Mountains, northeastern and southeastern U.S., but it becomes
35 lower over the central U.S. (e.g., Texas, Oklahoma, and Kansas). At night, however, most of
36 these regional differences between GFS and WRF are reversed. This diurnal difference is
37 mainly driven by the different PBL schemes employed in GFS (Han and Bretherton, 2019) and
38 WRF (i.e., YSU) and the associated other physical suites, including the land surface data. So this
39 PBL difference has strong regional variations depending on geographic differences. The GFS's
40 PBL height has a strong diurnal variation over these regions, including the western and

1 northeastern U.S. in the summer, including a sharp rise and collapse after sunrise and sunset,
2 respectively (Campbell et al., 2022). These two select times (18UTC and 06UTC) are not in the
3 transition period for PBL's fast diurnal changes. The strong PBL diurnal variation has significant
4 effects on the air quality predictions in GFS-CMAQ.
5

6 **3.2 Evaluation of Regional Meteorology and Air Quality against the AirNow Network**

7 The U.S EPA AirNow network provides hourly observations of near-surface ozone, fine
8 particulate matter (PM_{2.5}), and meteorology. Campbell et al. (2022) showed detailed verification
9 of GFS-CMAQ with the surface AIRNow data. Here we focus on the difference between the
10 interpolation-based GFSv16 versus WRF downscaling and the impacts on meteorological and
11 chemical model performances. Figure 3 shows a comparison of these two models over two
12 specific regions, the U.S. West (CA, OR and WA) and Northeast states (CT, DE, MA, MD, ME,
13 NH, NJ, NY, PA, RI, VT and District of Columbia) (Figure S1), where the two models had
14 relatively large differences for some meteorological variables. GFS and WRF had very similar 2-
15 m temperatures over the Pacific coast states: Washington, Oregon and California, and both of
16 them had similar cool bias (around 1K), R and RMSE (Figure 3a). However, these two models
17 had significant differences for the 10-m wind speed prediction over the Pacific coast (Figure 3c),
18 where WRF overpredicted the wind speed, especially at night and in later August. Most AIRNow
19 stations are located near urban or suburban areas, which generally have weaker 10-m wind speed
20 than those at the METAR aviation weather stations near airports. For this reason, although
21 Figure 1e and 1f shows that GFS and WRF underpredict monthly-mean wind speed over the
22 METAR stations in the West, they still tend to overpredict AIRNow wind (Figure 3c), especially
23 for the WRF 10-m wind speed at night. Considering that the model grid cells represent 12×12
24 km² averages, the true model-observation comparisons likely fall somewhere between the
25 urban/suburban AIRNow stations and METAR stations, depending on the land use fractions of
26 each grid. Obviously the observation representation characteristics could affect the verification
27 results. Compared to AIRNow stations, GFSv16 has overall better scores for surface wind speed
28 predictions over the U.S. West, where the WRF's larger surface wind speed overprediction is
29 associated with its PBL height predictions (Figure 3e, 3f). During the nighttime, GFS has a lower
30 PBL height (10–50% lower than WRF) and weaker vertical mixing, which brings less
31 momentum from the upper layers to the surface, which led to lower nighttime wind and better
32 agreements with the AIRNow wind-speed observation.
33

34 Over the northeast, the mean bias (MB) of GFS temperature was about -1K, while the WRF has
35 a smaller, slightly positive MB of about 0.22K (Figure 3b). However, the GFS's temperature
36 prediction has a better correlation coefficient, R, and RMSE, implying that it better captures
37 some events, such as the 28–29 of August. Both models overpredict 10-m wind speeds in the
38 northeast, but the GFS model yields better results due to a slightly lower PBLH at night (Figure
39 3f) than WRF that had significant overpredictions, especially during 25–29, August (Figure 3d)
40 when the tropical storm Erin approached this region. Especially on 28 of August, when the storm

1 was centered near the east coast of North Carolina, the WRF run significantly underpredicts 2-m
2 temperature (Figure 3b) and overpredict 10-m wind speed (Figure 3d), ~~implying that the some~~
3 ~~WRF settings lead to relatively large surface prediction bias for the storm weather. In the west~~
4 ~~around the same period, the tropical storm Ivo appeared in the southwest of the Baja California~~
5 ~~peninsula, and brought heavy rainfall in Mexico. Associated with this storm, a low pressure~~
6 ~~system expanded over most of the U.S. West. Differing from the GFSv16, which is designed for~~
7 ~~the operational meteorological forecast, the WRF configuration used in this study is normal for~~
8 ~~driving CMAQ, but not tuned for storm weather prediction, such as its relatively coarse vertical~~
9 ~~resolution compared to the 127-layer GFS model.~~

10
11 Figures 4a and 4b show the ozone predictions of the two models over these two regions, and
12 GFS-CMAQ yields predominantly lower O₃ than WRF-CMAQ, especially at night. Over the
13 ~~north~~west, the lower ozone in GFS-CMAQ is associated with their PBL height difference. First,
14 with a certain dry deposition velocity between the models, it is easier to deplete ozone given the
15 smaller volume of a shallower PBL. Second, the ~~thinner shallower~~ PBL results in higher NO_x
16 concentrations and ozone titration rates near NO_x source regions, and consequently lower ozone
17 there at night. Last, the lower PBL ~~could decouple from the residual layer, and leads result in to~~
18 ~~weaker or no vertical mixing and downward transport ozone exchange of with ozone from the~~
19 ~~residual layer at night (Caputi et al, 2019).~~ All these factors contributed to the lower nighttime
20 ozone of GFS-CMAQ compared to WRF-CMAQ. Since GFS-CMAQ already underpredicts
21 ozone due to combined meteorological factors, such as the temperature underprediction (Figure
22 4a), the GFS-CMAQ's further ozone reduction (possibly due to its lower PBLH at night)
23 exacerbates its low bias. However, over the Northeast, the similar impacts help the GFS-CMAQ
24 yield much better MB due to its better agreement with the observed nighttime low ozone over the
25 Northeast. Over the entire CONUS domain, the situation is similar: for an average August 2019,
26 the GFS-CMAQ has a lower ozone MB (1.1 ppb) compared to WRF-CMAQ (4.7 ppb). Figure 5
27 shows that both models have similar daytime ozone prediction over CONUS. However, GFS-
28 CMAQ better captures low nighttime ozone over the U.S. East than WRF-CMAQ (Figure 5c,
29 5d).

30
31 GFS-CMAQ has substantially higher PM_{2.5} mean concentrations over the U.S. West, but lower
32 over the U.S. Northeast compared to WRF-CMAQ (Figures 4c, 4d). These model differences are
33 also related to their interpolated GFSv16 versus downscaled WRF meteorological drivers.

34 Because both models use the same emissions under relatively clean background conditions in the
35 west (i.e., prevailing westerly flow from the Pacific Ocean), the PBL and wind speed differences
36 have significant impacts on their near-surface pollutant concentrations, especially at night. Both
37 models show strong PM_{2.5} diurnal variation (high at night and low during daytime), driven by
38 the meteorological diurnal variation (e.g. PBL), which overcomes the emission diurnal variation
39 (usually high during daytime and low at night). Compared to WRF-CMAQ, GFS-CMAQ has
40 lower nighttime PBL height and weaker wind speed at night, which leads to weaker vertical

1 mixing and venting, and increases the pollutant concentrations near the surface and yields higher
2 surface PM_{2.5} over the U.S. West (Figure 4c). Its higher surface PM_{2.5} could also result in
3 stronger local dry deposition. In contrast to local vertical mixing and venting effects on PM_{2.5}
4 discussed above, there are strong (and potentially counterbalancing) impacts of model PBL and
5 horizontal wind speed differences on downstream PM_{2.5} concentrations at night. WRF-CMAQ's
6 deeper PBL and stronger wind speeds at night (Figures 3c–3f) tends to transport aerosols and
7 their precursors more efficiently downstream via the dominant advection pathway. Figure 6
8 shows that these monthly mean background PM_{2.5} differences appear in East of Rocky
9 Mountain (WRF-CMAQ is about 2 µg/m³ higher) during both daytime and nighttime. This effect
10 is very prominent in the Northeast region. Although both models predicted similar PM_{2.5}
11 magnitude over the U.S. Northeast, GFS-CMAQ yields the overall PM_{2.5} underprediction, and
12 its monthly-mean PM_{2.5} is 2.6 µg/m³ lower than the WRF-CMAQ prediction (Figure 4d).
13 Especially during 01–09 August, WRF-CMAQ had about 4 µg/m³ higher surface PM_{2.5}
14 background than that of GFS-CMAQ. In this case, the WRF-CMAQ model has a better
15 agreement with observations (Figure 4d). It is possible that the GFS-CMAQ's nighttime PBL
16 heights (wind speeds) are too shallow (weak) in this case, which does not allow enough transport
17 of pollutants to the downstream (Eastern USA). Overall, GFS-CMAQ and WRF-CMAQ have
18 mixed performances for PM_{2.5} predictions during the August 2019 period: GFS-CMAQ has
19 better PM_{2.5} prediction over the U.S West, and WRF-CMAQ yields better results over east of
20 Rocky mountain (Figure 6).

21 **4 Model Comparisons against the FIREX-AQ Aircraft Data**

22 From late July to early September, 2019, the joint NOAA-NASA FIREX-AQ field campaign
23 (<https://csl.noaa.gov/projects/firex-aq/>) employed a suite of satellites, aircraft, vehicles and
24 ground site platforms aimed to observe, analyze, and characterize air pollutants emitted from
25 wildfire sources over the CONUS (Ye et al., 2021). The FIREX-AQ airborne measurements
26 provide a three-dimensional dataset from various meteorological, gas, and aerosol instruments
27 that is used to verify the GFS-CMAQ and WRF-CMAQ model performance, while elucidating
28 reasons for any model differences. Here the focus of the FIREX-AQ model comparison and
29 verification is against observations taken primarily from the NASA DC-8 aircraft, which include
30 meteorological variables, gaseous and aerosol concentrations, and aerosol optical properties
31 [merged in one-minute temporal resolution](#)-. [The model data are spatiotemporally interpolated to](#)
32 [the flight paths for comparison](#). The majority of the FIREX-AQ flights were over the western
33 United States, and sampled within environments that both were *and* were not (see section 4.1)
34 influenced by wildfire emissions
35 (https://daac.ornl.gov/MASTER/guides/MASTER_FIREX_AQ_JulySept_2019.html). During a
36 cluster of major wildfire events (see Section 4.2), the DC-8 sampled both near-source and aged
37 smoke plumes between 02–08 August, 2019 (i.e., the Williams Flats, Snow Creek, and Horsefly
38 Fires) across the states of Idaho, Washington, and Montana.
39

1 4.1 Comparison of the July 22 non-wildfire event over the central California Valley

2 On 22 July, the DC-8 aircraft flew from California to Boise, Idaho, while maintaining a
3 relatively low-altitude (<1 km) above sea level (ASL) over the California Central Valley (Figure
4 7). This flight was not impacted by any major wildfire event, and was mainly controlled by
5 anthropogenic emissions and local meteorological conditions. Figure 7 shows that the GFSv16
6 and WRF models had similar meteorological temperature and humidity predictions, and that both
7 models have dry and warm biases over the Central Valley at lower altitudes (Figures 7d–7e)
8 (Yun et al., 2020). GFS’s horizontal wind speeds tended to have stronger variability than WRF
9 (Figure 7b), especially in high altitudes. For wind direction, WRF showed a better prediction
10 than GFS around 20 and 24 UTC (Figure 7c).

11
12 Both GFS-CMAQ and WRF-CMAQ underestimate the vertical wind (W) variability by at least
13 one order of magnitude, and WRF-CMAQ has weaker W variability than that of GFS-CMAQ,
14 especially in high altitudes (Figure 7f). The model vertical velocities are not from the GFS or
15 WRF model, but rather they are re-diagnosed in CMAQ to conserve mass (Otte and Pleim,
16 2010), and thus represent the whole layer’s vertical movement across the 12 km by 12 km grid
17 cell. With its flight speed around 80 to 240 m/s, the DC-8 aircraft’s one-minute average
18 sampling frequency results in an approximate 4.8 to 14 km horizontal scale, respectively, which
19 is comparable to the 12 km CMAQ model resolution. The aircraft observations, however, include
20 turbulence effects during its one-minute averages, which may not be temporally resolved by
21 CMAQ at this resolution. Thus, both the GFS-CMAQ and WRF-CMAQ model vertical
22 velocities are much lower and have almost no correlation with the aircraft observations.

23
24 Although both GFS-CMAQ and WRF-CMAQ have reasonable comparisons for most
25 meteorological variables, including the horizontal winds, it continues to be a challenge to
26 compare them with the observed vertical velocities. Thus to further elucidate the model vs.
27 observation differences in vertical motions, Figure 8 shows a curtain plot of vertical velocities
28 along the flight path from the two models. Since WRF-CMAQ remains in a native grid, its wind
29 fields tend to be more balanced and have lower variability compared to the ~~interpolated~~-GFS-
30 CMAQ wind fields. The stronger variability in W for GFS-CMAQ ~~represents-could be caused by~~
31 GFS’s non-hydrostatic dynamics or CMAQ’s effort to counteract mass inconsistency effects
32 from the interpolated horizontal wind fields (Byun, 1999b). Our comparison shows that the first
33 factor should be the major one (Figure S2), as the GFS-CMAQ diagnosed W is very similar to
34 that from the original GFSv16 around 1km above the ground. As the original GFS has similarly
35 stronger W than WRF, the W difference between GFS-CMAQ and WRF-CMAQ is not due to
36 interpolation error of horizontal winds.

37
38 GFS-CMAQ and WRF-CMAQ overall yield similar results for specific chemical species during
39 this DC-8 flight (Figure 9). Both models underestimate CO, O₃ and ethane (C₂H₆) concentrations
40 over the lower altitudes in the California Central Valley. Over the same flight segment, they had

1 better NO_x (NO + NO₂) and ethene (C₂H₄) predictions, implying that the emissions of these two
2 species have better accuracy than those of CO and ethane. Figure 9f shows that the two models
3 also underestimate NO_z (NO_y-NO_x), or the oxidized nitrogen species besides NO_x, indicating
4 that the photochemical ozone production may also be underestimated. NO_z is a good indicator of
5 the ozone photochemical formation (Sillman et al., 1997), where the O₃/NO_z ratio represents the
6 ozone photochemical efficiency per NO_x oxidation products. Thus, NO_z and O₃ are typically
7 highly correlated over regions with active photochemical production. Our later analysis shows
8 that the models tend to underestimate certain hydrocarbons, such as ethane, which is likely
9 linked to the O₃ and NO_z underestimations, since they are likely due to the underestimation of CO
10 and some hydrocarbons, such as ethane, as they are the hydrocarbons are photochemical precursors
11 of O₃ and NO_z.
12

13 The two models show slight differences in peak values of CO, ethene, and NO_x around 23:30
14 UTC, where the GFS-CMAQ predicted concentrations are slightly higher and closer to
15 observations (Figure 9). These differences are due to their PBL predictions (both from the
16 corresponding meteorological model outputs), where GFS-CMAQ has a lower PBL height and
17 weaker emission vertical dilution compared to WRF-CMAQ (Figure 8). GFS-CMAQ tends to
18 underpredict O₃ more (Figure 9b), however, due to its higher NO_x titration. This implies that the
19 effects of the transport and non-local transformation of O₃ could be stronger than that of local
20 precursor emissions. WRF-CMAQ has higher NO_z (Figure 9f), but lower NO_x compared to
21 GFS-CMAQ due to the time lag of O₃ and NO_z photochemical formation. Consequently, the
22 peak O₃ values may not be well correlated with the emitted precursors, such as NO_x and volatile
23 organic compounds (VOCs). Furthermore, the modeled peak C₂H₆ and C₂H₄ concentrations do
24 not occur at the same time around 23:30 UTC, while observations indicate that these two species
25 should be highly correlated in this region. This model mismatch implies that the VOC speciation
26 factors for a certain area or emission sector need to be improved over Southern California.
27

28 **4.2 Comparison of the 6 August wildfire events over the U.S. Northwest**

29 On 06 August, the DC-8 observed a cluster of three wildfires: the Williams Flats Fire (47.98 °N,
30 118.624 °W, 80 km to the northwest of Spokane, Washington), Snow Creek Fire (47.703°N,
31 113.4°W, 32 km northeast of Condon, Montana), and Horsefly Fire (46.963 °N, 112.441°W, 24
32 km east of Lincoln, Montana). Figure 10a shows the flight path on that date, where the DC-8
33 aircraft departed from Boise, ID, flew over the Williams Flats Fire region, then flew to Montana
34 to sample the Snow Creek and Horsefly Fires (i.e., Montana Fires), and finally returned to the
35 Boise base. The aircraft flew below 8 km for most flight segments near the fire plumes. Figure
36 S1 shows the corresponding GOES-16 satellite true color image, where these 06 August fires and
37 associated smoke plumes are visible and can be distinguished from the cloud bands to the south
38 that move northward later that day (Figure S2S3). The Williams Flats Fire was ignited by
39 lightning, and was the largest fire event sampled during the FIREX-AQ campaign burning from
40 about 02–08, August, 2019.

1
2 Both models significantly underpredicted CO (Figure 10c), submicron organic aerosol (Figure
3 10e) and aerosol optical extinction coefficient (AOE) (Figure 10f), which suggests an issue with
4 the GBBEPx gas and aerosol emissions. The models performed well for NO₂ during the
5 Williams Flats and Montana Fires Fire below 6 km ASL, but there were prominent
6 underestimations for the high-altitude flight segments (Figure 10d). ~~However, since the NO₂~~
7 ~~instrument (The NOAA NOyO3 4-channel chemiluminescence) had NO₂ detection limit around~~
8 ~~0.01 ppb~~
9 ~~(https://airbornescience.nasa.gov/sites/default/files/documents/NOAA%20NOyO3_SEAC4RS.p~~
10 ~~df), the models might not truly underestimate NO₂ for these flight segments with extremely low~~
11 ~~NO₂. This indicates that the background NO₂ was underestimated, or the models had~~
12 ~~insufficient inject height for fire plume rise (both based on Briggs, 1965). WRF-CMAQ~~
13 predicted higher O₃ values than the GFS-CMAQ, which overall agreed better with observations
14 for the Williams Flats Fire (Figure 10b). However, for the Montana Fires (~ 23–24 UTC), WRF-
15 CMAQ has higher O₃ biases and GFS-CMAQ yields better results. The difference in O₃ is
16 largely driven by the regional background concentration difference between the two models,
17 where WRF-CMAQ tends to have higher domain-wide O₃ than GFS-CMAQ due to the
18 meteorological effects discussed in the S₃ sections 3 even they used the same lateral boundary
19 conditions.

20
21 Figure ~~S3-S4~~ shows the spatial overlay comparison of vertically averaged GFS-CMAQ
22 predictions at 21 UTC and the DC-8 flight observations for the altitude 1–3 km above ground
23 level (AGL), on 6 August, 2019. The peak NO₂ observation around 118.5°W, 48°N indicates the
24 general location of the Williams Flats fire. The GBBEPx emission and GFS-CMAQ prediction
25 showed shifted peak-value locations driven by the westerly modeled winds. For this flight, the
26 GBBEPx had stronger NO_x fire emission over two Montana locations than that over Williams
27 Flats. The model overpredicts the column averaged NO₂ concentrations, especially over the
28 Montana fires, which can not be reflected by the point-by-point NO₂ comparison result in Figure
29 10d. For this flight, the mean GFS-CMAQ NO₂ along the flight path for 1–3km AGL is about
30 0.125 ppbv compared to the observed mean NO₂ of 0.169 ppbv, and the model indeed showed
31 NO₂ underprediction along the flight path. However, in this case, the flight path ~~missed some~~
32 ~~locations where did not encounter the locations with~~ modeled peak NO₂ values ~~existed or as~~ the
33 ~~modeled transport~~ misplaced the plumes, especially over the Montana fires leading to this
34 inconsistency. For ozone comparison (Figure ~~S3bS4b~~), this inconsistency could also exist,
35 though not as significant as for the high-gradient NO₂ concentrations. In the GFS-CMAQ
36 prediction, the high ozone concentrations are almost co-located with high NO₂ concentration
37 (Figure ~~S3bS4b~~), but the observation did not show this feature. Instead, some high-O₃ flight
38 segments had relatively low NO₂, such as those circled in the black rectangle box of Figure
39 ~~S3bS4b~~. The observed NO_x titration was not able to be produced by the 12 km models. Wang et
40 al (2021) used a 100m horizontal resolution large eddy simulation and demonstrated the

Formatted: Subscript

Formatted: Subscript

Formatted: Subscript

Formatted: Subscript

1 capability of using such techniques to capture some high-resolution fire plume features and
2 associated chemical behavior. While such high resolution techniques are not currently feasible
3 for the operational NAQFC, they demonstrate the limitation of using regional scale (12×12 km)
4 models to capture such fine scale features of plume behavior.

5
6 GFS-CMAQ has higher wildfire-related CO, NO₂, OA and AOE values that are closer to
7 observations than WRF-CMAQ for the Montana Fires between 23–24 UTC at flight altitudes of
8 ~ 4–5 km (Figure 10c–10f). Since these two models use the same GBBEPx emissions and
9 wildfire plume rise algorithm (Briggs, 1965), the differences should be due to other reasons. To
10 help explain these model differences, Figure 11a and 11b show the Differential Absorption High
11 Spectral Resolution Lidar (DIAL-HSRL) retrieved aerosol backscatter coefficients (ABC)
12 aboard the DC-8 aircraft without and with cloud screen, respectively. It shows that the major fire
13 plumes of the Williams Flats Fire were below 4 km (~ 19–22 UTC), but the Montana Fires (~23–
14 24 UTC) extended from the surface up to 6 km, with some detached plumes reaching 10 km. The
15 model predicted AOE have an overall similar pattern, with major plumes below 4 km for the
16 Williams Flats Fire (Figures 11c and 11d). Over the Montana Fires, the GFS-CMAQ predicts
17 slightly higher PBL, thus allowing for the fire plume to reach a higher height near the DC-8
18 cruising altitude. In contrast, the WRF-CMAQ wildfire plumes are slightly lower than the
19 aircraft flight path around 23–24 UTC, which leads to underprediction in the fire emitted species
20 (Figure 11d).

21
22 An interesting feature in the DIAL observations is the detached plume from 8 km to 10 km
23 altitude (Figure 11a), where some cirrus clouds existed, and the DIAL retrieval could not
24 distinguish whether they are pure clouds or clouds mixed with elevated aerosols above 8km. The
25 cloud screen product (Figure 11b) mainly showed the enhanced aerosols below 7km and some
26 scattered signals near the high cloud edges. Cloud mixing with aerosols was usual for fire
27 induced clouds, or pyrocumulonimbus (Peterson et al., 2021). Although in this event, the middle-
28 size fires did not show evident of inducing the high-altitude clouds, the indicator of mixed clouds
29 and aerosols in high altitudes still existed: both in-situ measured OA (Figures 10e) and AOE
30 (Figure 10f, 11c, 11d) showed the enhanced aerosols around 25 UTC (or 1 UTC of the next day)
31 above 8km. This elevated plume was generally captured by the GFS-CMAQ simulation, while
32 underestimating its strength (Figure 11c); however, this feature was completely missed in WRF-
33 CMAQ (Figure 11d). Considering the altitude range of the detached plume, the major model
34 disparities are likely due to model convection differences in the free troposphere. To further
35 investigate this impact, Figures 11e and 11f show curtain plots of RH predicted by the two
36 models. GFS-CMAQ yields higher RH at such altitudes (10 km) compared to WRF-CMAQ
37 around 23–24 UTC, indicating that the GFS-CMAQ has stronger convection. The CMAQ model
38 uses inputted meteorology to diagnose convection activity and drive its ACM2 convection
39 scheme. This convective activity is apparent in GOES-16 satellite images (Figure ~~S2S3~~), as more
40 fractional clouds appeared ahead of the northward moving frontal band. Both the GFSv16 and

1 WRF models used here *do not* consider the fire heat feedback effect, and thus their predicted
2 convection and clouds are only driven by the synoptic weather conditions. If such synoptic-to-
3 mesoscale weather models consider wildfire heat feedback effects, their predictions may result in
4 stronger convection and help correct underpredictions in PBL heights.
5

6 **4.3 Statistical Results of Model Performances for FIREX-AQ**

7 4.3.1 *Meteorological Statistics*

8

9 During the FIREX-AQ field campaign, the DC-8 aircraft performed more than 20 flights over
10 CONUS with detailed observations of various chemical compounds. Tables 2 and 3 show the
11 statistical results of mean bias (MB), normalized mean bias (NMB), root mean square error
12 (RMSE), correlation coefficient (R), and linear regression/slopes for the two models'
13 performance over the western U.S. (west of 110°W) only at low altitudes (<3km ASL) for both
14 non-fire and fire flight segments. The FIREX-AQ aircraft data included the smoke flag to mark
15 the sampling times associated with fire plumes, identified by carbon monoxide and aerosol
16 enhanced over background levels in downwind area of specific fires. This smoke flag is used to
17 distinguish the flight segments with and without fire influences. Most of these flights departed
18 from Boise, ID, except the 22 July flight that flew from California to Idaho. As a result, they
19 mainly flew over Idaho and its surrounding regions. The GFS tends to have slightly higher wind
20 speed with positive MB, while WRF has a small negative wind speed bias. Most of the DC-8
21 flights are during the daytime, and the GFS has a higher daytime wind speed than WRF at low
22 altitudes. The GFS and WRF have very similar temperature predictions. For the RH, the GFS
23 predictions were slightly dryer than those of WRF, especially for non-fire events. The
24 meteorological models do not consider wildfire heat effects, and thus may have (in part) led to
25 slightly warm MB for the non-fire events (Table 2) and slightly cool MB for the fire events
26 (Table 3). Because both the GFSv16 and WRF models have similar MB shifts from an average
27 temperature overprediction (Table 2; non-fire events) to an underprediction (Table 3; wildfire
28 events), we can estimate that the fire effects made roughly a 1–2 Kelvin temperature
29 enhancement to the background along the DC-8 flight paths below 3 km. This estimate assumes
30 that the model temperature biases are generally representative of the western U.S. (west of
31 110°W), and are independent of the averaged flight segments that have different locations and
32 periods in Table 2 and Table 3. Correspondingly, the air masses are dryer in the sampled
33 wildfire plumes, as shown by the large reduction in the RH underpredictions (i.e., negative MBs)
34 from Table 2 to Table 3.
35

36 4.3.2 *Chemical Statistics* ~~*During for Non-Fire-Flight Segments without Fire Influences Events*~~

37

38 For most chemical species, the two models also have similar performance, indicating that the
39 emissions and chemistry are major driving forces. For ~~non-fire flight segments not encountering~~
40 ~~fire plumes events~~, both models overpredict NO_x, HNO₃, toluene, EC, and ammonium (NH₄⁺),

1 but underestimate PAN, benzene, C₂H₂, SO₂, and submicron sulfate and organic aerosols (OA)
2 (Table 2). The SO₂ and submicron sulfate underprediction may be impacted by underestimated
3 NEIC2016v1 SO₂ emissions over the western U.S. Since point sources, including power plant
4 emissions, are the SO₂ sources, this comparison implies that the point sources for 2019 events
5 have large uncertainties.

6
7 Although the models agree well with NO_y observations, they disproportionately underestimate
8 NO_z (non-NO_x reactive nitrogen species, or NO_y-NO_x) as shown by the regression slopes and
9 MBs. The NO_x and NO_y observations have different missing data, and NO_z is calculated when
10 both NO_x and NO_y observations are available at certain sampling times. Due to the different
11 sample number issues, their observed averages may not exactly match well (avaeraged
12 NO_x+NO_z ≠ NO_y), though their corresponding modeled relationship are well balanced. Gaseous
13 NO_z species can be split into inorganic NO_z, such as HNO₃, HONO, HNO₄, NO₃, ClNO₃, N₂O₅,
14 and organic NO_z, such as PAN, methyl peroxy acetyl nitrate (MPAN) and RNO₃ (or NTR, the
15 other organic nitrate) et al. The precursors of organic NO_z include hydrocarbons. One of the
16 important organic NO_z species is PAN, and both models underestimate PAN during for the flight
17 segments without non-fire events-influences (Table 2). -PAN's carbonyl precursors include
18 acetaldehyde (CH₃CHO) (44% of the global source), methylglyoxal (30%), acetone (7%), and a
19 suite of other isoprene and terpene oxidation products (19%) (Fischer et al., 2014). CH₃CHO and
20 acetone are also underestimated (Table 2), and help explain PAN's underestimation. For the
21 oxidized hydrocarbons, like aldehydes (HCHO, CH₃CHO), their main atmospheric sources are
22 the oxidation of highly reactive VOCs, including alkanes, alkenes, and aromatics, instead of
23 direct emissions (Parrish et al., 2012). So, the underestimation of HCHO and CH₃CHO are
24 associated with the underestimation of their precursor hydrocarbons, including anthropogenic
25 and biogenic VOCs. Our ether-internal comparison with some limited surface VOC observations
26 indicated that BEIS tends to underpredict biogenic emission over the U.S. West, e.g. isoprene in
27 Table 2. In this comparison, most anthropogenic hydrocarbons are disproportionately
28 underestimated, except toluene, implying the VOC speciation issue in the NEIC2016v1
29 anthropogenic emissions (Table 2). Previous work had discovered that a model overprediction in
30 toluene was also related to the toluene speciation in the NEI emission inventory (Lu et al., 2020).
31 In this comparison, both models tend to underpredict organic NO_z, which is likely caused by the
32 underestimation of certain VOCs.

33
34 Submicron (aerosol diameter < 1 μm) ammonium (NH₄⁺) and ~~the~~ nitrate ion (NO₃⁺) are also
35 underestimated by both models during non-fire events (Table 2), suggesting there are NH₃
36 underestimates due to either insufficient NH₃ emissions or exaggerated NH₃ removal processes.
37 There are, however, overpredictions in the intermediate species nitric acid (HNO₃~~-~~), indicating
38 the shift of gas-aerosol equilibrium partition of the nitrate ion. It implies that the HNO₃
39 accumulates in the atmosphere because the modeled NO_x and inorganic NO_z (such as NO₃)

Formatted: Subscript

Formatted: Subscript

Formatted: Subscript

Formatted: Subscript

Formatted: Subscript

Formatted: Subscript

Formatted: Subscript

Formatted: Superscript

Formatted: Subscript

1 pathways toward the nitrate ion and organic ~~nitrate aerosol products~~NO_x are reduced due to their
2 other precursor (NH₃ and VOCs) underestimation.

3
4 There are underestimations in the VOC and CO concentrations, which contributes to the ozone
5 underestimation during non-fire ~~events-flight segments~~ (Table 2). These non-fire comparisons
6 also highlight that both models have similar biases due to similar meteorology (Section 4.3.1),
7 and the use of the same anthropogenic emissions (NEIC2016v1), BEIS biogenic emission and
8 chemical models/mechanisms (i.e CMAQv5.3.1). The differences in the two models' bias, error,
9 and correlation/slope are much smaller than their individual magnitudes. As discussed above,
10 VOC speciation in the emission inventory could be one issue, as the model tends to overpredict
11 C₂H₄, but underestimate C₂H₂ and C₂H₆ etc. Some common biases over certain region could be
12 related to certain issues. For instance, some power plants supposed to shut down in the original
13 NEIC 2016 inventory might still emit pollutants during the flight observations, leading to the
14 disagreement of SO₂.

15 16 4.3.3 Chemical Statistics ~~During-for Flight Segments with Fire Events~~Influences

17
18 The WRF-CMAQ and GFS-CMAQ models significantly underestimate CO, VOC, HONO, and
19 OA for fire-~~influenced-flight segments~~ ~~events~~ at low altitudes (< 3 km) over the western U.S.
20 (Table 3). In conjunction with underestimated GBBEPx emissions during these wildfire events,
21 other possible causes for the average statistical underprediction are the CMAQ model's 12 km
22 horizontal resolution and the flight sampling coverage. Most of the fires that are averaged in the
23 statistics, such as the Horsefly (5.5 km² burning area) and Snow Creek Fires (7.3 km² burning
24 area), are at a much finer scale than the model grid. Only the largest Williams Flats Fire, with a
25 total burning area of 180 km² (Ye et al., 2021), had a comparable horizontal scale to the model
26 resolution.

27
28 The DC-8 aircraft had many flight segments near wildfire sources during the fire events in Table
29 3, and thus dilution of the emissions due to the relatively coarse model resolution may lead to
30 underestimations in the predicted slope for most wildfire emitted pollutants, such as CO and OA
31 (Table 3). The O₃ concentrations are also underestimated; however, the O₃ underpredictions are
32 reduced from the non-fire (Table 2) to fire events (Table 3). Abundant amounts of wildfire
33 emitted NO_x can titrate ozone near the fire source region, and the models likely underestimate
34 these titration effects due to the 12 km model resolution (Figure S4). Thus, the models cannot
35 capture the strong spatial O₃ variability that is observed due to both reduction near source
36 regions and enhancement in downstream areas. Again, for this fire event comparison, both
37 models showed similar behavior and their differences were relatively smaller compared to the
38 overall model biases.

Formatted: Subscript

Formatted: Subscript

Formatted: Subscript

Formatted: Subscript

Formatted: Subscript

Formatted: Subscript

Formatted: Subscript

Formatted: Subscript

1 5. Summary and Discussion

2 The operational NOAA/NWS National Air Quality Forecasting Capability (NAQFC) recently
3 underwent a major upgrade on July 20, 2021. The advanced NAQFC includes the recent
4 Community Multi-scale Air Quality (CMAQ) model version 5.3.1 with CB6 (carbon bond
5 version 6)-Aero7 (version 7 of the aerosol module) chemical mechanism, and is driven by the
6 latest operational Finite Volume Cubed-Sphere (FV3)-Global Forecast System, version 16
7 (GFSv16) (Campbell et al., 2022). Here we analyze the impacts of the driving meteorological
8 models on CMAQ model performance with the new GFSv16 interpolation-based meteorology
9 versus the commonly-used native-grid Weather Research and Forecasting (WRF) model version
10 4.0.3 meteorology. The meteorological and chemical analysis includes both 2D ground-based
11 and 3D aircraft measurements during the summer 2019, which encompasses the joint NOAA-
12 NASA Fire Influence on Regional to Global Environments and Air Quality (FIREX-AQ)
13 campaign. As CMAQ has existing mass conservation via adjustments of the contravariant
14 vertical velocity (Otte and Pleim, 2010), the NACC interpolated GFSv16 wind field can be well
15 handled in CMAQ (i.e., GFS-CMAQ).

16
17 The different NWS/NOAA operational GFS and commonly chosen WRF physics schemes
18 employed in this study (Table 1) clearly have impacts on temperature, horizontal/vertical wind
19 fields (~~both horizontal/advection and vertical/convection~~), PBL heights, and the corresponding
20 CMAQ model predictions. During this study period over the U.S. West, both models showed
21 moisture dry bias and temperature warm bias in low altitudes, which could be due to the issue
22 mentioned by Qian et al (2020): the irrigation contribution being neglected (section 3.1), and
23 impacts from soil moisture deficits on surface fluxes in both models. Due to their different
24 physics, GFS had stronger diurnal variation of PBL height, lower at night and higher during
25 daytime over the U.S. West and Northeast. The differences in the GFS and WRF physics have a
26 larger impact than the ~~meteorology driver methodologies difference (i.e., between interpolation~~
27 interpolated vs. and native grids on the models' meteorological and air quality predictions, even
28 despite using FDDA to nudge WRF simulation toward the GFSv16 data. While FDDA nudging
29 was used here in WRF to avoid growing errors across a continuous 1-month simulation, we note
30 that if it is turned off, the differences between GFSv16 and WRF predictions would have been
31 even greater. This would further substantiate the dominance of using different model physics
32 ~~compared to using different meteorological driver methodologies (i.e., native vs. interpolation)~~
33 and their impacts on CMAQ model predictions. Campbell et al (2022) have the detailed
34 comparisons for interpolated and original fields, and they are very consistent. In this study, we
35 further compare the CMAQ vertical velocity diagnosed from on interpolated GFS horizontal
36 wind, which is very consistent with the original GFS vertical velocity. Overall, the results of this
37 study further corroborate the use of the GFSv16 data and NACC interpolation-based methods
38 (Campbell et al., 2022) for regional CMAQ model applications in the scientific community.

39

1 Over CONUS, GFS-CMAQ demonstrated lower mean surface ozone (by about 3 ppb) and
2 PM_{2.5} (by about 1 μg/m³) than WRF-CMAQ in August 2019 (section 3). In the western U.S.,
3 the GFS has a stronger diurnal variability in PBL height and a better performance in nighttime
4 10-m wind speeds compared to WRF. The nighttime difference between these two models tends
5 to be more significant than the corresponding daytime difference. Their difference is also
6 impacted by both vertical/convective (mainly daytime) and upstream advective transport
7 differences in GFS-CMAQ and WRF-CMAQ, which somewhat confounds the impact of
8 different meteorological physics on chemical predictions from region to region. This transport
9 effect is more significant on PM_{2.5} than that on O₃, as O₃ has a shorter lifetime and is more
10 sensitive to local emissions in summer. In this study, neither GFS-CMAQ nor WRF-CMAQ
11 show overwhelming performance advantage over the other, similar to the NMM-CMAQ and
12 ARW-CMAQ comparison in Yu et al. (2012a, 2012b).

13
14 GFS-CMAQ and WRF-CMAQ demonstrated rather similar performance for major chemical
15 variables during both FIREX-AQ non-fire (Table 2) and fire events (Table 3). In most FIREX-
16 AQ events, both GFS-CMAQ and WRF-CMAQ showed similar biases, indicating that other
17 factors, including emissions, model resolution and chemistry etc. could be more important for the
18 model predictions compared to the meteorological differences. The aircraft data comparison
19 reveals many common issues in both model systems. One critical issue is whether the flight
20 sampling coverage is comparable to the 12 km model resolution, especially for high-gradient fire
21 emission, e.g. the case of 06 August flight (Figure S3S4). The observation representation issue
22 also exists in other places, such as near-surface meteorological comparison between AIRNow
23 stations and METAR stations. Emission is the driving force for atmospheric composition
24 concentrations. The comprehensive aircraft measurements help verify that the anthropogenic
25 NEIC2016v1 inventory is overall reasonable, except for SO₂, NH₃ and certain hydrocarbons. The
26 wildfire emission has bigger uncertainties, including the emission intensities, specification and
27 plume rise, shown by the both models' results.

28
29 The NACC interpolation method is advantageous as it enables using the original meteorological
30 driver directly via interpolation, and avoids running another model such as WRF ~~as a downscaler~~
31 ~~for to drive~~ regional CMAQ applications. It is also faster, and more consistent with the original
32 meteorological ~~driver model (GFS) than using WRF with nudging, since WRF's own physics~~
33 ~~could have stronger impact.~~ In current NOAA/NCEP operational GFS-CMAQ system, NACC
34 only takes less than 5 minutes to process 72-hour data, which saves enough time for CMAQ to
35 forecast extra 24 hours. These aspects can simultaneously benefit real-time forecasting and
36 retrospective air quality applications in the scientific community. NACC can also adapt to
37 quickly use any regional domain globally, and may also use other global meteorological data
38 including reanalysis products. This helps mitigate the confounding factors of using different
39 model configurations across the myriad of WRF physics options, while alleviating the difficulty
40 in understanding their impacts on air quality predictions. The operational GFSv16 and associated

1 reanalysis products are well vetted and evaluated across different global agencies and
2 laboratories, and thus are well suited for regional CMAQ applications using NACC. In fact, there
3 is an ongoing project at NOAA to migrate both the GFSv16 data and NACC software to the
4 Amazon Web Services (AWS) Cloud platform to provide a streamlined product for the user to
5 generate the model-ready meteorological data for any regional CMAQ application globally.

6
7 Finally, we note that the current operational GFSv16 has ~~enough all needed~~ meteorological
8 variables to drive CMAQ ~~with, and users have option to other supplied supply other~~ data
9 (fractional landuse, LAI etc), ~~and, its GFSv16's C768 grid has horizontal resolution from 10.21~~
10 ~~km to 14.44 km, which is close to the NAQFC's 12 km horizontal resolution. One barrier of~~
11 ~~using this NACC approach is that the original-resolution GFS data with all needed variables are~~
12 ~~in very big even with compression (about 8Gb per time step), and may not be available to~~
13 ~~community users. There is an ongoing effort of using cloud storages to solve this issue, and~~
14 ~~making this method available to the community. Traditional WRF-CMAQ usually starts from~~
15 ~~However, some~~ commonly available global meteorological data, such as NCEP or ECMWF
16 reanalysis data, ~~which are in relatively coarse resolution, and use WRF to generate may not have~~
17 ~~all meteorological variables needed by CMAQ in native grid, and have relatively coarse model~~
18 ~~resolutions. In this some cases, the WRF downscaling may become the only available method to~~
19 ~~drive a finer scale CMAQ model application. WRF's various data generated by different physics~~
20 ~~may be good for can also be customized for a finer scale CMAQ simulation over certain regions~~
21 ~~or under certain meteorological conditions. Both methods have its pros and cons. however~~
22 ~~NACC developments are underway to also process/interpolate higher resolution FV3 based~~
23 ~~Limited Area Models (LAMs) for direct application to CMAQ. All the physics schemes were~~
24 ~~developed according to certain regions and meteorological conditions. We again stress, however,~~
25 ~~that the downscaled WRF physics may significantly alter the original meteorological fields even~~
26 ~~with the FDDA nudging. As shown in this study, GFS and WRF had mixed performance for~~
27 ~~driving CMAQ, though they are overall similar.~~

28 **Code and Data Availability.**

29 The FIREX-AQ field campaign data used in this study is in [https://www-air.larc.nasa.gov/cgi-](https://www-air.larc.nasa.gov/cgi-bin/ArcView/firexq)
30 [bin/ArcView/firexq](https://www-air.larc.nasa.gov/cgi-bin/ArcView/firexq) (last access, 16 May 2022). The NACC code used in this study is publicly
31 available at <https://doi.org/10.5281/zenodo.5507489> and via GitHub at [https://github.com/noaa-](https://github.com/noaa-oar-arl/NACC.git)
32 [oar-arl/NACC.git](https://github.com/noaa-oar-arl/NACC.git) (last access: 5 April 2022). The modified CMAQv5.3.1 for GFS-CMAQ is
33 available at <https://doi.org/10.5281/zenodo.5507511> and via GitHub at [https://github.com/noaa-](https://github.com/noaa-oar-arl/NAQFC)
34 [oar-arl/NAQFC](https://github.com/noaa-oar-arl/NAQFC) (last access: 5 April 2022).

35 **Author contributions.**

36
37 YT contributed to the project conceptualization, model run, software, data analysis, visualization,
38 investigation, and writing of the original draft. PCC contributed to software, the model run, data
39 analysis, investigation and draft revision. DT and XZ contributed to wildfire emissions data. BB

1 contributed to software and funding acquisition. FY, JH and HH provided the GFS model data.
2 LP provided the global aerosol model for the lateral boundary condition. PL, RS, AS, JF, IS, JT-
3 D, YJ contributed to project supervision, project administration, and funding acquisition. MY,
4 IB, JF, TR, DB, JS, J-LJ, JC, GD, RM, JH, GH, AR and JD contributed to the FIREX-AQ
5 aircraft data.

7 **Competing interests.**

8 The contact author has declared that neither they nor their co-authors have any competing
9 interests.

11 **Acknowledgements**

12 This research was funded by NOAA's National Air Quality Forecasting Capability (NAQFC) in
13 the National Weather Service Office of Science and Technology Integration (NWS/OSTI).

15 **References:**

- 16 Appel, K.W., Bash, J.O., Fahey, K.M., Foley, K.M., Gilliam, R.C., Hogrefe, C., Hutzell, W.T.,
17 Kang, D., Mathur, R., Murphy, B.N. and Napelenok, S.L., The Community Multiscale Air
18 Quality (CMAQ) model versions 5.3 and 5.3. 1: system updates and evaluation. *Geoscientific*
19 *Model Development*, 14(5), pp.2867-2897. 2021. <https://doi.org/10.5194/gmd-14-2867-2021>
- 20 Arakawa, A. and Lamb, V.: Computational design of the basic dynamical processes of the
21 UCLA general circulation model, *Methods in Computational Physics*, 17, 173–265, 1977.
- 22 Baker, K.R., Woody, M.C., Tonnesen, G.S., Hutzell, W., Pye, H.O.T., Beaver, M.R., Pouliot, G.
23 and Pierce, T., Contribution of regional-scale fire events to ozone and PM_{2.5} air quality
24 estimated by photochemical modeling approaches. *Atmospheric Environment*, 140, 539-554.
25 <https://doi.org/10.1016/j.atmosenv.2016.06.032>, 2016.
- 26 Briggs, G. A., A Plume Rise Model Compared with Observations, *Journal of the Air Pollution*
27 *Control Association*, 15:9, 433-438, doi:10.1080/00022470.1965.10468404, 1965.
- 28 Byun, D. W., Dynamically Consistent Formulations in Meteorological and Air Quality Models
29 for Multiscale Atmospheric Studies. Part I: Governing Equations in a Generalized Coordinate
30 System, *Journal of the Atmospheric Science*, 56, 3789–3807. 1999a.
31 [https://doi.org/10.1175/1520-0469\(1999\)056<3789:DCFIMA>2.0.CO;2](https://doi.org/10.1175/1520-0469(1999)056<3789:DCFIMA>2.0.CO;2)
- 32 Byun, D.W., Dynamically consistent formulations in meteorological and air quality models for
33 multi-scale atmospheric applications: Part II. Mass conservation issues. *Journal of the*
34 *Atmospheric Science* 56, 3808–3820, 1999b. [https://doi.org/10.1175/1520-](https://doi.org/10.1175/1520-0469(1999)056<3808:DCFIMA>2.0.CO;2)
35 [0469\(1999\)056<3808:DCFIMA>2.0.CO;2](https://doi.org/10.1175/1520-0469(1999)056<3808:DCFIMA>2.0.CO;2).
- 36 Byun, D.W., Ching, J.K.S.. Science algorithms of the EPA models-3 Community Multiscale Air
37 Quality (CMAQ) modeling system, EPA/600/R-99/030, U.S. EPA. 1999c

- 1 Byun, D. and Schere, K.L., Review of the governing equations, computational algorithms, and
2 other components of the Models-3 Community Multiscale Air Quality (CMAQ) modeling
3 system. *Appl. Mech. Rev.* 59: 51–77. <https://doi.org/10.1115/1.2128636>. 2006.
- 4 Campbell, P., Tang, Y., Lee, P., Baker, B., Tong, D., Saylor, R., Stein, A., Huang, J., Huang, H.-
5 C., Strobach, E., McQueen, J., Pan, L., Stajner, I., Sims, J., Tirado-Delgado, J., Jung, Y.,
6 Yang, F., Spero, T., and Gilliam, R.: Development and evaluation of an advanced National
7 Air Quality Forecast Capability using the NOAA Global Forecast System version 16, *Geosci.*
8 *Model Dev.* 15, 3281–3313, <https://doi.org/10.5194/gmd-15-3281-2022>, 2022.
- 9 Chen, F., and Dudhia, J. Coupling an advanced land surface-hydrology model with the Penn
10 State-NCAR MM5 modeling system. Part I: Model implementation and sensitivity. *Monthly*
11 *Weather Review*, 129(4), 569–585. 2001. [https://doi.org/10.1175/1520-](https://doi.org/10.1175/1520-0493(2001)129<0569:CAALSH>2.0.CO;2)
12 [0493\(2001\)129<0569:CAALSH>2.0.CO;2](https://doi.org/10.1175/1520-0493(2001)129<0569:CAALSH>2.0.CO;2)
- 13 Chen J.-H and S.-J Lin. The remarkable predictability of inter-annual variability of atlantic
14 hurricanes during the past decade. *Geophysical Research Letters*, 38(L11804):6, 2011.
15 <https://doi.org/10.1029/2011GL047629>
- 16 Chen J.-H. and S.-J. Lin. Seasonal predictions of tropical cyclones using a 25-km-resolution
17 general circulation model. *J. Climate*, 26(2):380–398, 2013. [https://doi.org/10.1175/JCLI-D-](https://doi.org/10.1175/JCLI-D-12-00061.1)
18 [12-00061.1](https://doi.org/10.1175/JCLI-D-12-00061.1)
- 19 Clough, S. A., Shephard, M. W., Mlawer, J. E., Delamere, J. S., Iacono, M. J., Cady-Pereira, K.,
20 et al. (2005). Atmospheric radiative transfer modeling: A summary of the AER codes. *Journal*
21 *of Quantitative Spectroscopy & Radiative Transfer*, 91(2), 233–244.
22 <https://doi.org/10.1016/j.jqsrt.2004.05.058>
- 23 Caputi, D. J., Faloona, I., Trousdell, J., Smoot, J., Falk, N., and Conley, S.: Residual layer ozone,
24 mixing, and the nocturnal jet in California's San Joaquin Valley, *Atmos. Chem. Phys.*, 19,
25 4721–4740, <https://doi.org/10.5194/acp-19-4721-2019>, 2019
- 26 Dong, X., J. S. Fu, K. Huang, D. Tong, and G. Zhuang. Model development of dust emission
27 and heterogeneous chemistry within the Community Multiscale Air Quality modeling system
28 and its application over East Asia. *Atmos. Chem. Phys.*, 16, 8157–8180. 2016.
29 <https://doi.org/10.5194/acp-16-8157-2016>.
- 30 Ek, M. B., Mitchell, K. E., Lin, Y., Rogers, E., Grunmann, P., Koren, V., et al. (2003).
31 Implementation of Noah land surface model advances in the National Centers for
32 Environmental Prediction operational mesoscale Eta model. *Journal of Geophysical Research*,
33 108(D22), 8851. <https://doi.org/10.1029/2002JD003296>
- 34 Fischer, E. V., Jacob, D. J., Yantosca, R. M., Sulprizio, M. P., Millet, D. B., Mao, J., Paulot, F.,
35 Singh, H. B., Roiger, A., Ries, L., Talbot, R. W., Dzepina, K., and Pandey Deolal, S.:
36 Atmospheric peroxyacetyl nitrate (PAN): a global budget and source attribution, *Atmos.*
37 *Chem. Phys.*, 14, 2679–2698, <https://doi.org/10.5194/acp-14-2679-2014>, 2014.
- 38 Fu, X., S. X. Wang, Z. Cheng, J. Xing, B. Zhao, J. D. Wang, and J. M. Hao, 2014: Source,
39 transport and impacts of a heavy dust event in the Yangtze River Delta, China, in 2011.
40 *Atmos. Chem. Phys.*, 14, 1239–1254, doi:10.5194/acp-14-1239-2014.

1 Grell, G. A., Dudhia, J., and Stauffer, D. R. A description of the fifth-generation Penn
2 State/NCAR Mesoscale Model (MM5). NCAR tech. Note NCAR TN-398-1-STR, 117 pp.
3 1994.

4 Han, J., & Bretherton, C. S., TKE-Based Moist Eddy-Diffusivity Mass-Flux (EDMF)
5 Parameterization for Vertical Turbulent Mixing, *Weather and Forecasting*, 34(4), 869-886.
6 2019. <https://doi.org/10.1175/WAF-D-18-0146.1>

7 Harris, L., Chen, X., Putman, W., Zhou, L. and Chen, J.H., A Scientific Description of the GFDL
8 Finite-Volume Cubed-Sphere Dynamical Core. <https://doi.org/10.25923/6nhs-5897>. 2021

9 Hodyss, D. and N. Nichols, The error of representation: basic understanding, *Tellus A: Dynamic*
10 *Meteorology and Oceanography*, 67:1, <https://doi.org/10.3402/tellusa.v67.24822>, 2015.

11 Hong, Song-You, Yign Noh, Jimy Dudhia, A new vertical diffusion package with an explicit
12 treatment of entrainment processes. *Mon. Wea. Rev.*, 134, 2318–2341. 2006.
13 doi:10.1175/MWR3199.1.

14 Houyoux, M.R., Vukovich, J.M., Coats, C.J., Wheeler, N.J.M., Kasibhatla, P.S., Emission
15 inventory development and processing for the seasonal model for regional air quality
16 (SMRAQ) project. *J. Geophys. Res.*, 105(D7), 9079-9090,
17 <https://doi.org/10.1029/1999JD900975>. 2000.

18 Huang, M., D. Tong, P. Lee, L. Pan, Y. Tang, I. Stajner, R. B. Pierce, J. McQueen, and J. Wang,
19 Toward enhanced capability for detecting and predicting dust events in the western United
20 States: The Arizona case study. *Atmos. Chem. Phys.*, 15, 12 595–12 610, doi:10.5194/acp-15-
21 12595-2015. 2015.

22 Kain, J. S., The Kain–Fritsch convective parameterization: An update. *J. Appl. Meteor.*, 43, 170–
23 181. doi:10.1175/1520-0450(2004)043<0170:TKCPAU>2.0.CO;2, 2004.

24 Kim, Y.J., Eckermann, S.D. and Chun, H. Y., An overview of the past, present and future of
25 gravity-wave drag parameterization for numerical climate and weather prediction models.
26 *Atmosphere-Ocean*, 41(1), 65-98., doi: 10.3137/ao.410105, 2003.

27 Krueger, S. K., Q. Fu, K. N. Liou, and H-N. S. Chin. Improvement of an ice-phase microphysics
28 parameterization for use in numerical simulations of tropical convection. *Journal of Applied*
29 *Meteorology*, 34:281–287, January 1995. <https://doi.org/10.1175/1520-0450-34.1.281>

30 Iacono, M. J., Delamere, J. S., Mlawer, E. J., Shephard, M. W., Clough, S. A., and Collins, W.
31 D.. Radiative forcing by long-lived greenhouse gases: Calculations with the AER radiative
32 transfer models. *Journal of Geophysical Research*, 113, D13103. 2008.
33 <https://doi.org/10.1029/2008JD009944>

34 Jimenez, P. A., Dudhia, J., Gonzalez-Rouco, J. F., Navarro, J., Montavez, J. P., & Garcia-
35 Bustamante, E. (2012). A revised scheme for the WRF surface layer formulation. *Monthly*
36 *Weather Review*, 140(3), 898–918. <https://doi.org/10.1175/MWR-D-11-00056.1>

37 Lin, Y.-L., R. D. Farley, and H. D. Orville. Bulk parameterization of the snow field in a cloud
38 model. *J. Climate Appl. Meteor.*, 22:1065–1092, 1983. [https://doi.org/10.1175/1520-
39 0450\(1983\)022<1065:BPOTSF>2.0.CO;2](https://doi.org/10.1175/1520-0450(1983)022<1065:BPOTSF>2.0.CO;2)

- 1 Lord, S. J., H.E. Willoughby, and J.M. Piotrowicz. Role of a parameterized ice-phase
2 microphysics in an axisymmetric, nonhydrostatic tropical cyclone model. *J. Atmos. Sci.*,
3 41(19):2836–2848, October 1984. [https://doi.org/10.1175/1520-](https://doi.org/10.1175/1520-0469(1984)041<2836:ROAPIP>2.0.CO;2)
4 [0469\(1984\)041<2836:ROAPIP>2.0.CO;2](https://doi.org/10.1175/1520-0469(1984)041<2836:ROAPIP>2.0.CO;2)
- 5 Lu, Q., Murphy, B. N., Qin, M., Adams, P. J., Zhao, Y., Pye, H. O. T., Efstathiou, C., Allen, C.,
6 and Robinson, A. L.: Simulation of organic aerosol formation during the CalNex study:
7 updated mobile emissions and secondary organic aerosol parameterization for intermediate-
8 volatility organic compounds, *Atmos. Chem. Phys.*, 20, 4313–4332,
9 <https://doi.org/10.5194/acp-20-4313-2020>, 2020
- 10 Luecken, D. J., Yarwood, G., and Hutzell, W. T.: Multipollutant modeling of ozone, reactive
11 nitrogen and HAPs across the continental US with CMAQ-CB6, *Atmos. Environ.*, 201, 62–
12 72, <https://doi.org/10.1016/j.atmosenv.2018.11.060>, 2019.
- 13 Mlawer, E. J., Taubman S. J., Brown P. D., Iacono M. J., and Clough S. A., Radiative transfer
14 for inhomogeneous atmospheres: RRTM, a validated correlated-k model for the longwave. *J.*
15 *Geophys. Res.*, 102, 16663–16682. 1997. <https://doi.org/10.1029/97JD00237>.
- 16 Monin, A. S., & Obukhov, A. M. Basic laws of turbulent mixing in the surface layer of the
17 atmosphere (in Russian). Contribution Geophysics Institute, Academy of Sciences USSR,
18 151, 163–187. 1954.
- 19 Morrison, H., G. Thompson, V. Tatarskii, 2009: Impact of Cloud Microphysics on the
20 Development of Trailing Stratiform Precipitation in a Simulated Squall Line: Comparison of
21 One- and Two-Moment Schemes. *Mon. Wea. Rev.*, 137, 991–1007.
22 <https://doi.org/10.1175/2008MWR2556.1>
- 23 National Emissions Inventory Collaborative (2019). 2016v1 Emissions Modeling Platform.
24 Retrieved from <http://views.cira.colostate.edu/wiki/wiki/10202>.
- 25 Ott, E., Hunt, B.R., Szunyogh, I., Zimin, A. V., Kostelich, E.J., Corazza, M., Kalnay, E., Patil,
26 D.J. and Yorke, J.A., 2004. A local ensemble Kalman filter for atmospheric data
27 assimilation. *Tellus A: Dynamic Meteorology and Oceanography*, 56(5), pp.415-428.
28 <https://doi.org/10.3402/tellusa.v56i5.14462>
- 29 Otte, T. L., J E. Pleim, and G Pouliot. PREMAQ: A new pre-processor to cmaq for air-quality
30 forecasting. Presented at 2004 Models-3 Conference, Chapel Hill, NC, October 18-20, 2004.
- 31 Otte, T. L. and Pleim, J. E.: The Meteorology-Chemistry Interface Processor (MCIP) for the
32 CMAQ modeling system: updates through MCIPv3.4.1, *Geosci. Model Dev.*, 3, 243–256,
33 <https://doi.org/10.5194/gmd-3-243-2010>, 2010.
- 34 Pan, L., Kim, H., Lee, P., Saylor, R., Tang, Y., Tong, D., Baker, B., Kondragunta, S., Xu, C.,
35 Ruminski, M. G., Chen, W., McQueen, J., and Stajner, I.: Evaluating a fire smoke simulation
36 algorithm in the National Air Quality Forecast Capability (NAQFC) by using multiple
37 observation data sets during the Southeast Nexus (SENEX) field campaign, *Geosci. Model*
38 *Dev.*, 13, 2169–2184, <https://doi.org/10.5194/gmd-13-2169-2020>, 2020.
- 39 Parrish, D. D., Ryerson, T. B., Mellqvist, J., Johansson, J., Fried, A., Richter, D., Walega, J. G.,
40 Washenfelder, R. A., de Gouw, J. A., Peischl, J., Aikin, K. C., McKeen, S. A., Frost, G. J.,

1 Fehsenfeld, F. C., and Herndon, S. C.: Primary and secondary sources of formaldehyde in
2 urban atmospheres: Houston Texas region, *Atmos. Chem. Phys.*, 12, 3273–3288,
3 <https://doi.org/10.5194/acp-12-3273-2012>, 2012.

4 Peterson, D.A., Fromm, M.D., McRae, R.H., Campbell, J.R., Hyer, E.J., Taha, G., Camacho,
5 C.P., Kablick, G.P., Schmidt, C.C. and DeLand, M.T., Australia’s Black Summer
6 pyrocumulonimbus super outbreak reveals potential for increasingly extreme stratospheric
7 smoke events. *npj Climate and Atmospheric Science*, 4(1), 2021.
8 <https://doi.org/10.1038/s41612-021-00192-9>

9 Poggio, L., de Sousa, L. M., Batjes, N. H., Heuvelink, G. B. M., Kempen, B., Ribeiro, E., and
10 Rossiter, D.: SoilGrids 2.0: producing soil information for the globe with quantified spatial
11 uncertainty, *SOIL*, 7, 217–240, 2021. <https://doi.org/10.5194/soil-7-217-2021>

12 Powers, J.G., Klemp, J.B., Skamarock, W.C., Davis, C.A., Dudhia, J., Gill, D.O., Coen, J.L.,
13 Gochis, D.J., Ahmadov, R., Peckham, S.E. and Grell, G.A., The weather research and
14 forecasting model: Overview, system efforts, and future directions. *Bulletin of the American
15 Meteorological Society*, 98(8), pp.1717-1737. 2017. <https://doi.org/10.1175/BAMS-D-15-00308.1>

16

17 Putman, W. M. and S.-J. Lin, Finite-volume transport on various cubed-sphere grids, *Journal of
18 Computational Physics*, 227(1), 55-78, <https://doi.org/10.1016/j.jcp.2007.07.022>, 2007.

19 Qian, Y., Yang, Z., Feng, Z., Liu, Y., Gustafson, W.I., Berg, L.K., Huang, M., Yang, B. and Ma,
20 H.Y., Neglecting irrigation contributes to the simulated summertime warm-and-dry bias in the
21 central United States. *npj Clim Atmos Sci* 3, 31. [https://doi.org/10.1038/s41612-020-00135-](https://doi.org/10.1038/s41612-020-00135-w)
22 [w](https://doi.org/10.1038/s41612-020-00135-w), 2020

23 [Rolph, G. D., Draxler, R. R., Stein, A. F., Taylor, A., Ruminski, M. G., Kondragunta, S., Zeng,
24 J., Huang, H. C., Manikin, G., McQueen, J. T., and Davidson, P. M.: Description and
25 Verification of the NOAA Smoke Forecasting System: The 2007 Fire Season, *Weather
26 Forecast.*, 24, 361–378. <https://doi.org/10.1175/2008waf2222165.1>, 2009.](https://doi.org/10.1175/2008waf2222165.1)

27 Skamarock, W. C., Klemp, J. B., Dudhia, J., Gill, D. O., Liu, Z., Berner, J., Huang, X.-Yu.. A
28 Description of the Advanced Research WRF Model Version 4. NCAR Tech Note,
29 NCAR/TN–556+STR. doi:10.5065/1dfh-6p97, 2021.

30 Skamarock, W.C., Snyder, C., Klemp, J.B. and Park, S.H., vertical resolution requirements in
31 atmospheric simulation. *Monthly Weather Review*, 147(7), 2641-2656.
32 <https://doi.org/10.1175/MWR-D-19-0043.1>, 2019.

33 Shi, Y., Hu, F., Xiao, Z., Fan, G. and Zhang, Z., Comparison of four different types of planetary
34 boundary layer heights during a haze episode in Beijing. *Science of the total environment*,
35 711, <https://doi.org/10.1016/j.scitotenv.2019.134928>, 2020.

36 Sillman, S., He, D., Cardelino, C., and Imhoff, R. E.: The use of photochemical indicators to
37 evaluate ozone-NO_x–hydrocarbon sensitivity: Case studies from Atlanta, New York, and Los
38 Angeles, *J. Air Waste Manage. Assoc.*, 47, 1030–1040,
39 doi:10.1080/10962247.1997.11877500, 1997.

1 Sofiev, M., Ermakova, T., and Vankevich, R.: Evaluation of the smoke-injection height from
2 wild-land fires using remote-sensing data, *Atmos. Chem. Phys.*, 12, 1995–2006,
3 <https://doi.org/10.5194/acp-12-1995-2012>, 2012.

4 Tewari, M., Chen, F., Wang, W., Dudhia, J., LeMone, M. A., Mitchell, K., et al. Implementation
5 and verification of the unified NOAA land surface model in the WRF model. Paper Presented
6 at the 20th Conference on Weather Analysis and Forecasting/16th Conference on Numerical
7 Weather Prediction, Seattle, WA, 2004.

8 Wang, S., Coggon, M.M., Gkatzelis, G.I., Warneke, C., Bourgeois, I., Ryerson, T., Peischl, J.,
9 Veres, P.R., Neuman, J.A., Hair, J. and Shingler, T., Chemical Tomography in a Fresh
10 Wildland Fire Plume: a Large Eddy Simulation (LES) Study. *Journal of Geophysical*
11 *Research: Atmospheres*, 126(18), <https://doi.org/10.1029/2021JD035203>. 2021

12 Yamartino, R. J., Nonnegative, conserved scalar transport using grid-cell-centered, spectrally
13 constrained Blackman cubics for applications on a variable-thickness mesh. *Mon. Wea. Rev.*
14 121, 753-763, 1999. [https://doi.org/10.1175/1520-493\(1993\)121<0753:NCSTUG>2.0.CO;2](https://doi.org/10.1175/1520-493(1993)121<0753:NCSTUG>2.0.CO;2)

15 Yang, F., Tallapragada, V., Kain, J. S., Wei, H., Yang, R., Yudin, V. A., Moorthi, S., Han, J.,
16 Hou, Y. T., Wang, J., Treadon, R., and Kleist, D. T. (2020). Model Upgrade Plan and Initial
17 Results from a Prototype NCEP Global Forecast System Version 16. 2020 AMS Conference,
18 Boston, MA. <https://ams.confex.com/ams/2020Annual/webprogram/Paper362797.html>

19 Yarwood, G., Jung, J., Whitten, G.Z., Heo, G., Mellberg, J. and Estes, M., Updates to the Carbon
20 Bond mechanism for version 6 (CB6). In 9th Annual CMAS Conference, Chapel Hill, NC
21 (pp. 11-13). 2010.

22 Yarwood, Y., Sakulyanontvittaya, T., Nopmongcol, O., and Koo, K.: Ozone depletion by
23 bromine and iodine over the Gulf of Mexico, final report for the Texas Commission on
24 Environmental Quality, available at:
25 [https://www.tceq.texas.gov/assets/public/implementation/air/am/contracts/reports/pm/582111](https://www.tceq.texas.gov/assets/public/implementation/air/am/contracts/reports/pm/5821110365FY1412-20141109-enviro-bromine.pdf)
26 [0365FY1412-20141109-enviro-bromine.pdf](https://www.tceq.texas.gov/assets/public/implementation/air/am/contracts/reports/pm/5821110365FY1412-20141109-enviro-bromine.pdf) (last access: 3 May 2021), November 2014.

27 Ye, X., Arab, P., Ahmadov, R., James, E., Grell, G. A., Pierce, B., Kumar, A., Makar, P., Chen,
28 J., Davignon, D., Carmichael, G. R., Ferrada, G., McQueen, J., Huang, J., Kumar, R.,
29 Emmons, L., Herron-Thorpe, F. L., Parrington, M., Engelen, R., Peuch, V.-H., da Silva, A.,
30 Soja, A., Gargulinski, E., Wiggins, E., Hair, J. W., Fenn, M., Shingler, T., Kondragunta, S.,
31 Lyapustin, A., Wang, Y., Holben, B., Giles, D. M., and Saide, P. E.: Evaluation and
32 intercomparison of wildfire smoke forecasts from multiple modeling systems for the 2019
33 Williams Flats fire, *Atmos. Chem. Phys.*, 21, 14427–14469, [https://doi.org/10.5194/acp-21-](https://doi.org/10.5194/acp-21-14427-2021)
34 [14427-2021](https://doi.org/10.5194/acp-21-14427-2021), 2021.

35 Yu, S., Mathur, R., Pleim, J., Pouliot, G., Wong, D., Eder, B., Schere, K., Gilliam, R. and Rao,
36 S.T. Comparative evaluation of the impact of WRF/NMM and WRF/ARW meteorology on
37 CMAQ simulations for PM_{2.5} and its related precursors during the 2006
38 TexAQS/GoMACCS study. *Atmospheric Chemistry and Physics*, 12(9), doi:10.5194/acp-12-
39 4091-2012, 2012a.

1 Yu, S., Mathur, R., Pleim, J., Pouliot, G., Wong, D., Eder, B., Schere, K., Gilliam, R. and Rao,
2 S.T., 2012. Comparative evaluation of the impact of WRF–NMM and WRF–ARW
3 meteorology on CMAQ simulations for O₃ and related species during the 2006
4 TexAQS/GoMACCS campaign. *Atmospheric Pollution Research*, 3(2), pp.149-162, doi:
5 10.5094/APR.2012.015, 2012b.

6 Zhang, X., and Kondragunta, S., 2006, Estimating forest biomass in the USA using generalized
7 allometric model and MODIS land data, *Geographical Research Letter*, 33, L09402,
8 doi:10.1029/2006GL025879.

9 Zhang, X., Kondragunta, S., and Quayle, B. Estimation of biomass burned areas using multiple-
10 satellite-observed active fires. *IEEE Transactions on Geosciences and Remote Sensing*, 49:
11 4469-4482, 10.1109/TGRS.2011.2149535, 2011.

12 Zhuang, J., Jacob, D. J., and Eastham, S. D.: The importance of vertical resolution in the free
13 troposphere for modeling intercontinental plumes, *Atmos. Chem. Phys.*, 18, 6039–6055,
14 <https://doi.org/10.5194/acp-18-6039-2018>, 2018.

15

1 Table 1. The two meteorological datasets used in this study

Model Settings	FV3-GFSv16/NACC	WRF-ARW/MCIP
Domain	Global C768L127 (~ 13 km horizontal resolution in 6 cubic spherical tiles , 127 vertical layers up to 80km), interpolated to the 12km CONUS domain with 35-layers up to about 14km (60hPa)	12km CONUS 35 vertical layers up to 100hPa
Dynamic core	Finite Volume 3, non-hydrostatic (Putman and Lin, 2007)	WRF-ARW dynamic in hybrid vertical coordinate (Skamarock et al., 2021)
Initial condition	FV3-GFSv16 analysis (GDAS) using the local ensemble Kalman filter (LETKF) (Ott et al., 2004) with 4-dimensional incremental analysis update (4D-IAU)	FV3-GFSv16 analysis (GDAS)
Lateral Boundary Condition	N/A	FV3-GFSv16 analysis (GDAS)
Cloud Microphysics	GFDL six-category cloud microphysics scheme (Lin et al., 1983; Lord et al., 1984; Krueger et al., 1995; Chen and Lin, 2011; Chen and Lin, 2013)	Morrison 2-moment scheme (Morrison et al., 2009)
PBL Physics Scheme	Scale-aware (sa) turbulent kinetic energy (TKE) -based moist eddy-diffusivity mass-flux (EDMF) (sa-TKE-EDMF) (Han and Bretherton, 2019)	Yonsei University Scheme (Hong et al., 2006)
Shallow/Deep Cumulus Parameterization	SAS Scheme (Han et al. 2011; 2017)	Kain Fritsch multiscale (Kain, 2004)
Shortwave and Longwave Radiation	RRTMG (Mlawer et al. 1997; Clough et al. 2005; Iacono et al. 2008)	RRTMG (Iacono et al. 2008).
Land Surface Model	Noah Land Surface Model (Chen and Dudhia 2001; Ek et al. 2003; Tewari et al. 2004)	Noah (Tewari et al., 2004)
Surface Layer	Monin-Obukhov (Monin-Obukhov 1954; Grell et al. 1994; Jimenez et al. 2012)	Revised MM5 Scheme (Jimenez et al., 2012)
Other treatment		FDDA nudging is enabled for temperature and specific humidity whole domain, and for wind components (U, V) outside the PBL.

2

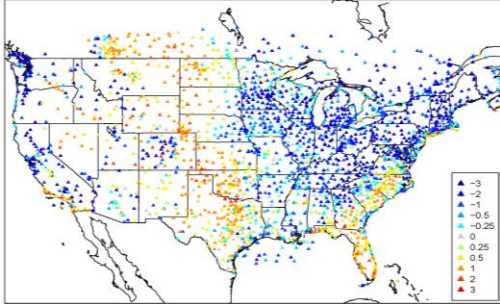
Variables	Obs Mean	GFS-CMAQ					WRF-CMAQ				
		MB	NMB	RMSE	R	Slope	MB	NMB	RMSE	R	Slope
Temperature (K)	295	0.979	0.332	2.04	0.988	1.13	1.16	0.393	2.28	0.989	1.17
RH (%)	35.6	-7.3	-20.5	11.8	0.781	0.717	-6.05	-17	12.6	0.677	0.598
Wind Speed (m/s)	4.81	0.758	15.8	3.25	0.432	0.473	-1.11	-23.1	2.4	0.666	0.524
O ₃ (ppbv)	57.9	-10.7	-18.5	15	0.651	0.34	-10.4	-17.9	14.1	0.717	0.413
CO (ppbv)	134	-37.6	-28	53.2	0.654	0.573	-37.1	-27.7	52.9	0.652	0.572
NO _x (ppbv)	1.11	0.507	45.6	2.9	0.704	1.15	0.345	31.1	2.86	0.695	1.12
NO _y (ppbv)	2.56	-0.0418	-1.63	3.07	0.743	0.892	0.055	2.15	3.14	0.724	0.86
NO _z (ppbv)	1.63	-0.465	-28.6	1.17	0.782	0.553	-0.125	-7.66	1.08	0.788	0.721
HONO (ppbv)	0.00432	0.012	279	0.0438	0.379	0.444	0.0134	311	0.0487	0.358	0.48
HNO ₃ (ppbv)	0.291	0.154	53.1	0.421	0.683	1.34	0.337	116	0.65	0.708	1.89
PAN (ppbv)	0.399	-0.251	-63	0.416	0.675	0.221	-0.222	-55.6	0.386	0.681	0.284
NH ₃ (ppbv)	3.55	-0.801	-22.6	5.26	0.0481	0.038	-1.58	-44.5	4.37	0.304	0.155
C ₂ H ₄ (ppbv)	0.121	0.0582	48.1	0.189	0.702	0.869	0.0385	31.9	0.187	0.682	0.836
C ₂ H ₂ (ppbv)	0.146	-0.0734	-50.3	0.137	0.784	0.496	-0.0696	-47.7	0.137	0.771	0.494
SO ₂ (ppbv)	0.342	-0.235	-68.8	0.567	0.0238	0.00835	-0.221	-64.5	0.568	-1.26×10 ⁻³	-0.00047
Acetone (ppbv)	2.74	-2.28	-83.1	2.45	0.686	0.192	-2.2	-80.4	2.38	0.668	0.199
HCHO (ppbv)	2.1	-0.972	-46.4	1.26	0.559	0.447	-0.909	-43.4	1.25	0.513	0.442
CH ₃ CHO (ppbv)	0.736	-0.326	-44.2	0.538	0.647	0.386	-0.349	-47.4	0.554	0.643	0.38
Benzene (ppbv)	0.0449	-0.0193	-43	0.057	0.398	0.385	-0.0191	-42.6	0.0564	0.397	0.375
Toluene (ppbv)	0.039	0.0409	105	0.153	0.759	1.74	0.0352	90.1	0.14	0.762	1.63
Isoprene (ppbv)	0.073	0.0361	49.4	0.174	0.6	0.838	0.00661	9.06	0.145	0.648	0.797
EC (µg/std m ³)	0.108	0.191	177	0.572	0.518	2.09	0.228	211	0.609	0.455	1.88
OA (µg/std m ³)	10.9	-7.15	-65.7	9.72	0.565	0.263	-6.48	-59.5	9.45	0.495	0.243
Sulfate (µg/std m ³)	1.31	-0.781	-59.7	1.11	0.0856	0.0188	-0.773	-59	1.11	0.0322	0.00677
NH ₄ ⁺ (µg/std m ³)	0.745	-0.615	-82.5	0.805	0.416	0.103	-0.596	-79.9	0.778	0.509	0.145
Nitrate (µg/std m ³)	1.22	-1.08	-88.1	1.49	0.562	0.229	-1.04	-85.3	1.45	0.57	0.279
AOE (/Mm)	54.5	-29.3	-53.8	47	0.593	0.227	-27.4	-50.2	45.9	0.588	0.227

Table 2. Statistics of the two models compared to the observation for DC-8 flight segments with out non-fire events influences below 3km (ASL) over west of -100°W. All aerosols are in submicron. The normalized mean bias (NMB) is in unit %.

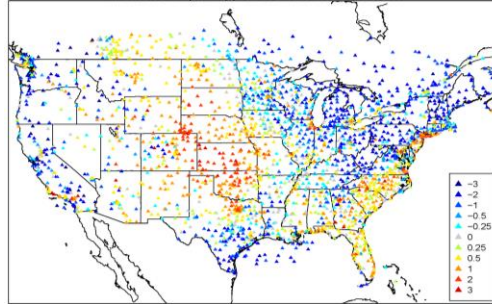
Variables	Obs Mean	GFS-CMAQ					WRF-CMAQ				
		MB	NMB	RMSE	R	Slope	MB	NMB	RMSE	R	Slope
Temperature (K)	287	-0.389	-0.135	0.702	0.995	1.01	-0.688	-0.24	0.863	0.997	1.04
RH (%)	27.8	-0.761	-2.74	7.84	0.712	0.553	4.3	15.5	11.1	0.556	0.534
Wind Speed (m/s)	5.42	0.766	14.1	2.16	0.612	0.616	-0.811	-15	2.12	0.604	0.556
O ₃ (ppbv)	55.7	-6.61	-11.9	11.8	0.587	0.262	-7.01	-12.6	11.5	0.653	0.346
CO (ppbv)	486	-377	-77.6	873	0.596	0.0347	-383	-78.8	883	0.442	0.0242
NO _x (ppbv)	2.63	0.06	2.28	6.41	0.465	0.231	-0.619	-23.5	7.02	0.31	0.153
NO _y (ppbv)	7.32	-4.19	-57.3	13.3	0.507	0.123	-4.66	-63.7	14.2	0.31	0.073
NO _z (ppbv)	5.7	-4.8	-84.3	10.2	-0.189	-0.0106	-4.68	-82	10.2	-0.204	-0.0121
HONO (ppbv)	0.283	-0.274	-96.8	1.18	0.355	0.0043	-0.274	-96.8	1.18	0.291	0.00457
HNO ₃ (ppbv)	0.148	0.148	99.7	0.256	0.532	1.07	0.179	121	0.28	0.402	0.768
PAN (ppbv)	0.971	-0.793	-81.7	1.63	0.27	0.0195	-0.765	-78.8	1.61	0.279	0.026
NH ₃ (ppbv)	17.7	-12.3	-69.3	28.3	0.379	0.0654	-13.7	-77.4	29.6	0.232	0.0386
C ₂ H ₄ (ppbv)	4.5	-4.34	-96.3	10.2	0.421	0.00498	-4.36	-96.8	10.2	0.14	0.0018
C ₂ H ₂ (ppbv)	1.04	-1.01	-96.9	2.08	0.534	0.00866	-1.01	-97	2.09	0.363	0.00623
SO ₂ (ppbv)	0.699	-0.322	-46.1	1.38	0.589	0.198	-0.392	-56.1	1.5	0.429	0.132
Acetone (ppbv)	3.54	-3.2	-90.3	4.56	0.13	0.00862	-3.18	-89.7	4.55	0.135	0.0112
HCHO (ppbv)	8.17	-7.13	-87.3	17.8	0.232	0.0062	-7.19	-88	17.8	0.119	0.00303
CH ₃ CHO (ppbv)	3.65	-3.18	-87.4	9.13	0.186	0.00547	-3.21	-88	9.2	-0.027	-0.00097
Benzene (ppbv)	0.683	-0.67	-98.1	1.84	0.54	0.00432	-0.672	-98.3	1.84	0.367	0.00275
Toluene (ppbv)	0.451	-0.436	-96.6	1.36	0.402	0.00491	-0.438	-97	1.36	0.195	0.00245
Isoprene (ppbv)	0.095	-7.9×10 ⁻³	-8.29	0.234	0.123	0.0579	-0.033	-34.7	0.242	-0.014	-0.00541
EC (µg/std m ³)	1.89	-0.53	-28	3.28	0.612	0.295	-0.787	-41.6	3.7	0.448	0.195
OA (µg/std m ³)	156	-146	-93.4	420	0.612	0.0174	-147	-94.2	423	0.472	0.0122
Sulfate (µg/std m ³)	0.791	-0.116	-14.7	0.676	0.415	0.184	-0.214	-27.1	0.728	0.322	0.13
NH ₄ ⁺ (µg/std m ³)	1	-0.591	-59.1	0.931	0.767	0.351	-0.615	-61.5	0.956	0.729	0.359
Nitrate (µg/std m ³)	1.7	-0.56	-32.9	1.47	0.805	0.613	-0.634	-37.2	1.59	0.774	0.599
AOE (Mm)	391	-350	-89.3	994	0.688	0.027	-357	-91.1	1010.	0.532	0.0152

Table 3, same as Table 2 except for the wildfire affected flight segments.

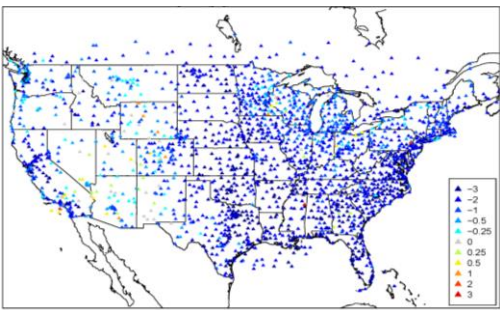
a) GFS mean 2m temperature bias (K), 08/2019



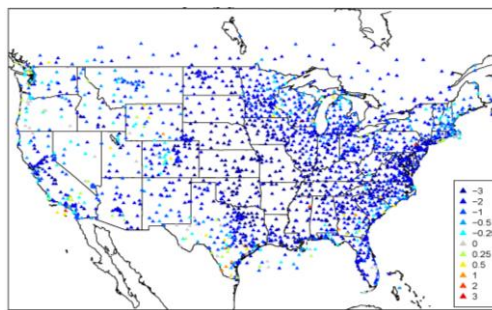
b) WRF mean 2m temperature bias (K), 08/2019



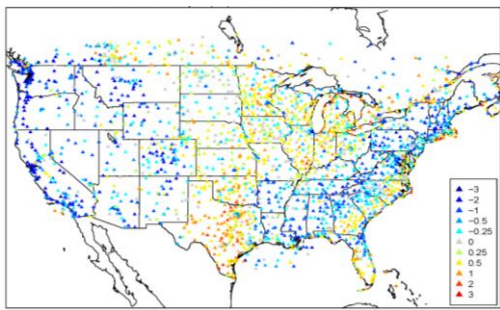
c) GFS mean 2m specific humidity bias (g/kg), 08/2019



d) WRF mean 2m specific humidity bias (g/kg), 08/2019



e) GFS mean 10m wind speed bias (m/s), 08/2019



f) WRF mean 10m wind speed bias (m/s), 08/2019

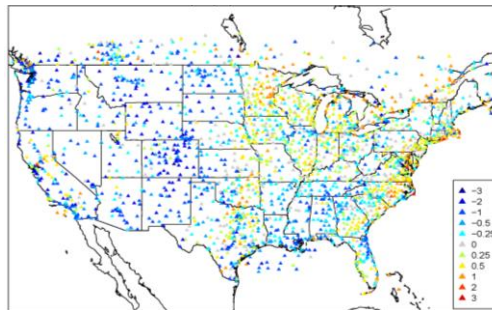
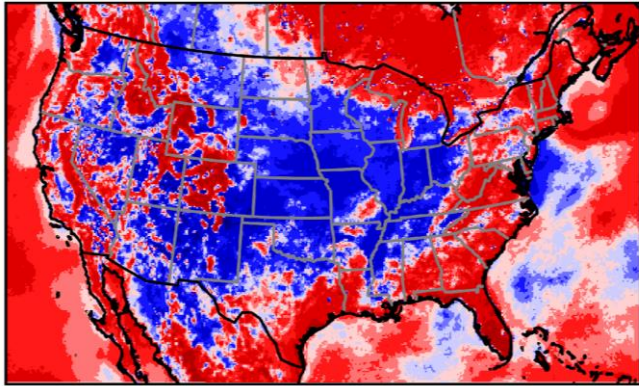


Figure 1. GFS and WRF surface meteorological biases for METAR (METeoro logical Aerodrome Report) stations averaged over August, 2019

a) Monthly Mean PBL Difference (GFS-WRF) at 18UTC



b) Monthly Mean PBL Difference (GFS-WRF) at 06UTC

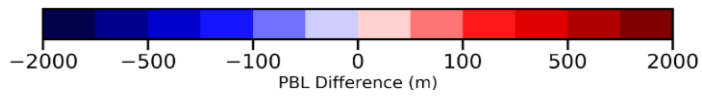
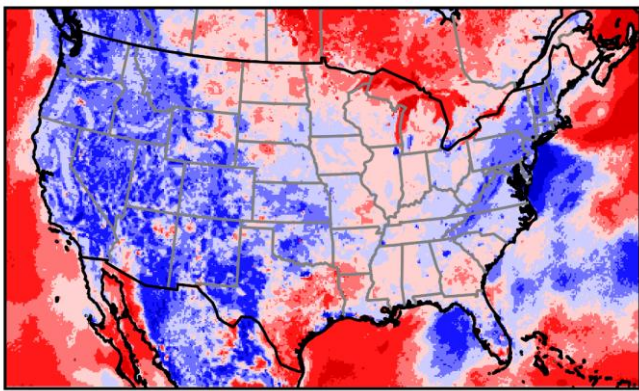


Figure 2. Monthly mean PBL height difference (GFS-WRF) for daytime (a) and nighttime (b), August, 2019.

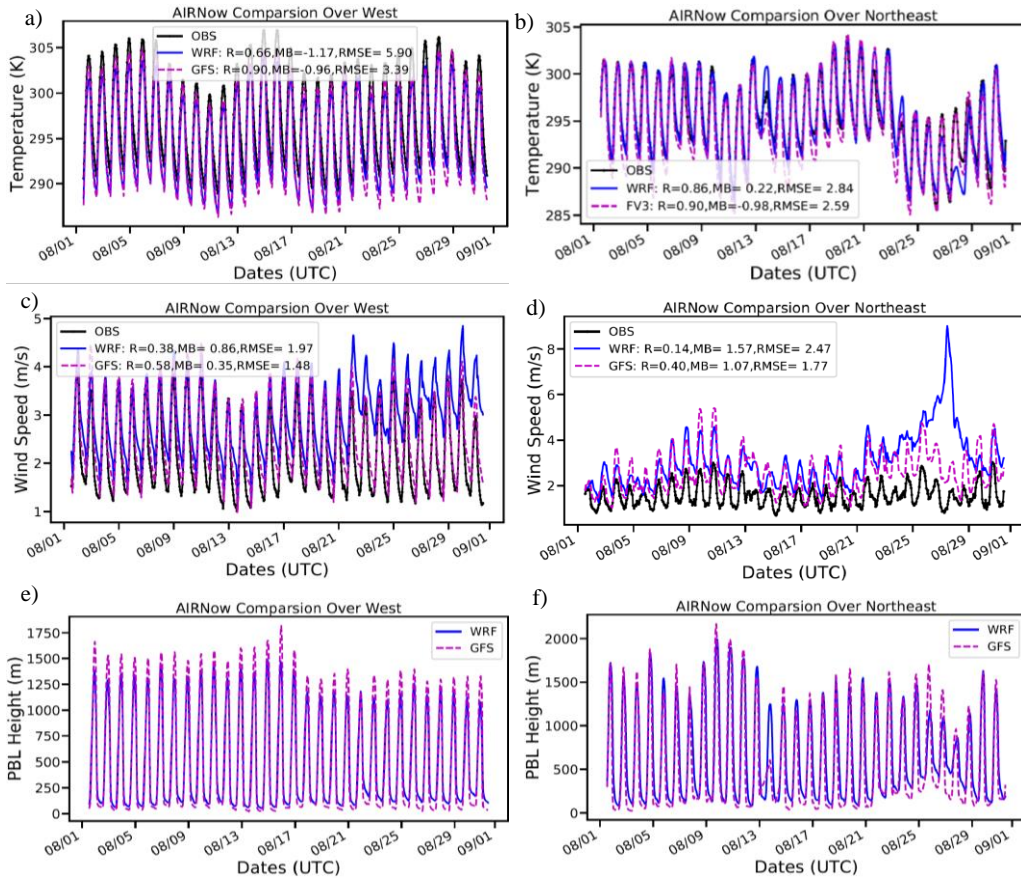


Figure 3. The WRF and GFS time-series comparison over AIRNow stations over the U.S. West and Northeast for 2m temperature (a, b), 10m wind speed (c, d), and PBL height (e,f).

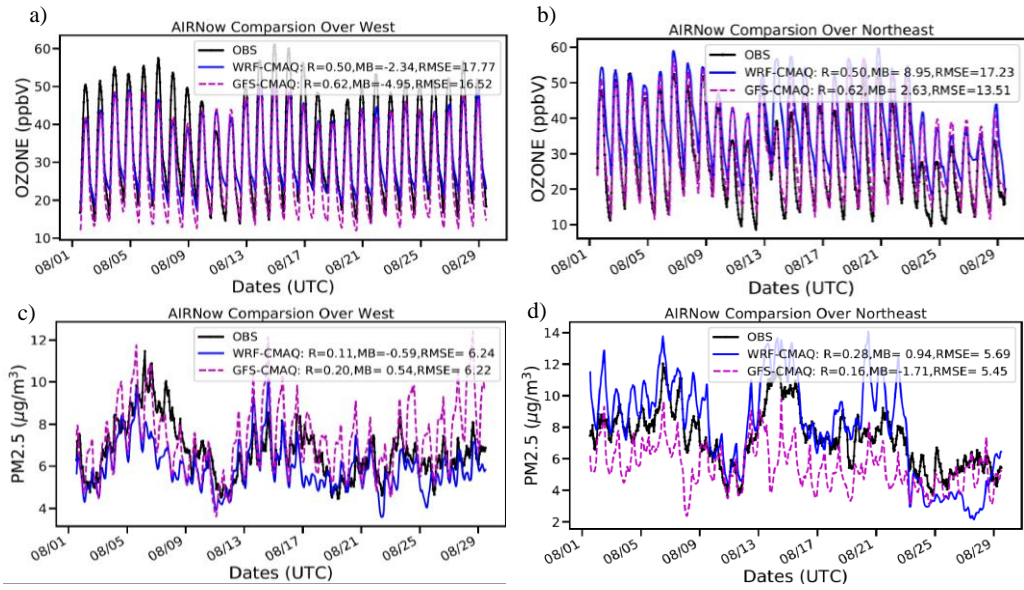


Figure 4. Same as Figure 3 but for ozone (a, b) and PM2.5 (c, d).

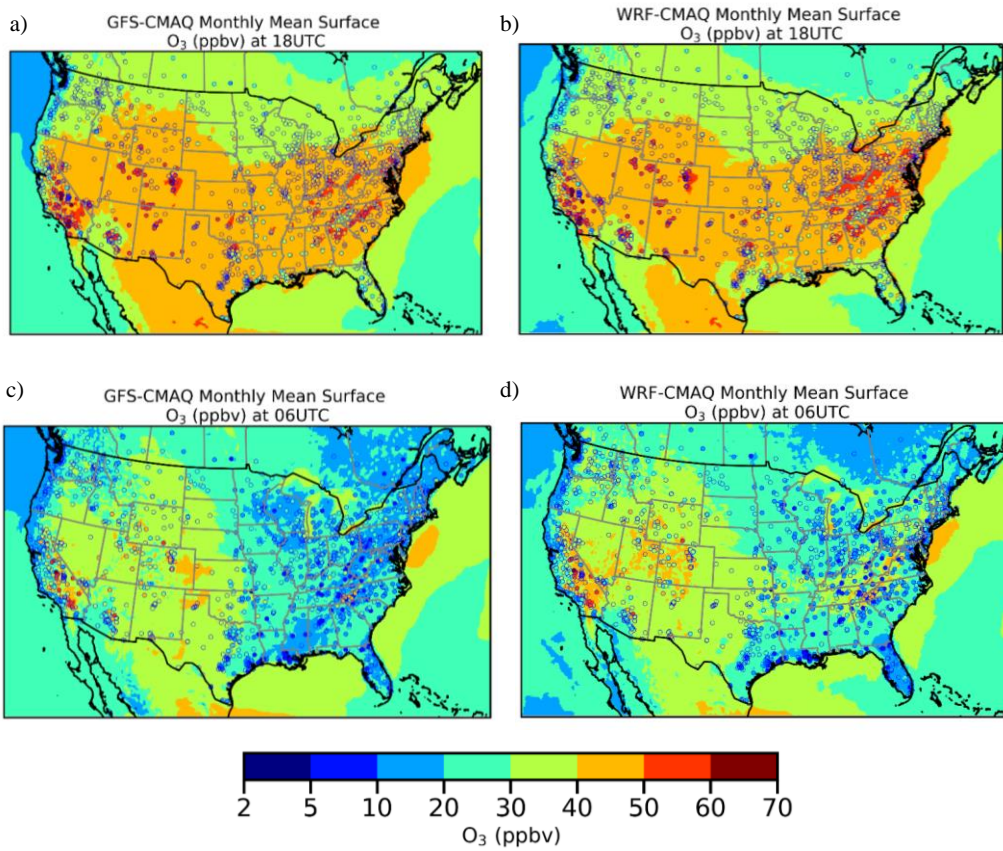


Figure 5. Monthly mean surface ozone predictions by GFS-CMAQ (left plots) and WRF-CMAQ (right plots) for daytime (top plots) and nighttime (bottom plots) compared to the corresponding AIRNow observations, August, 2019

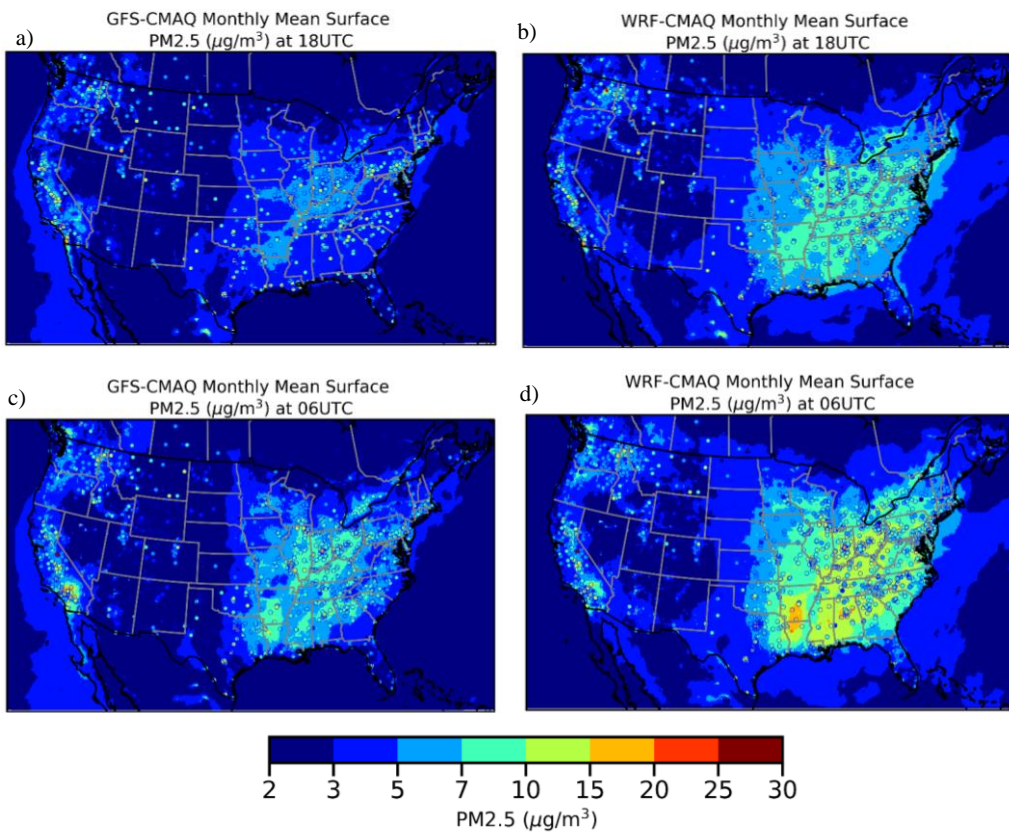


Figure 6, same as figure 5 but for surface PM2.5

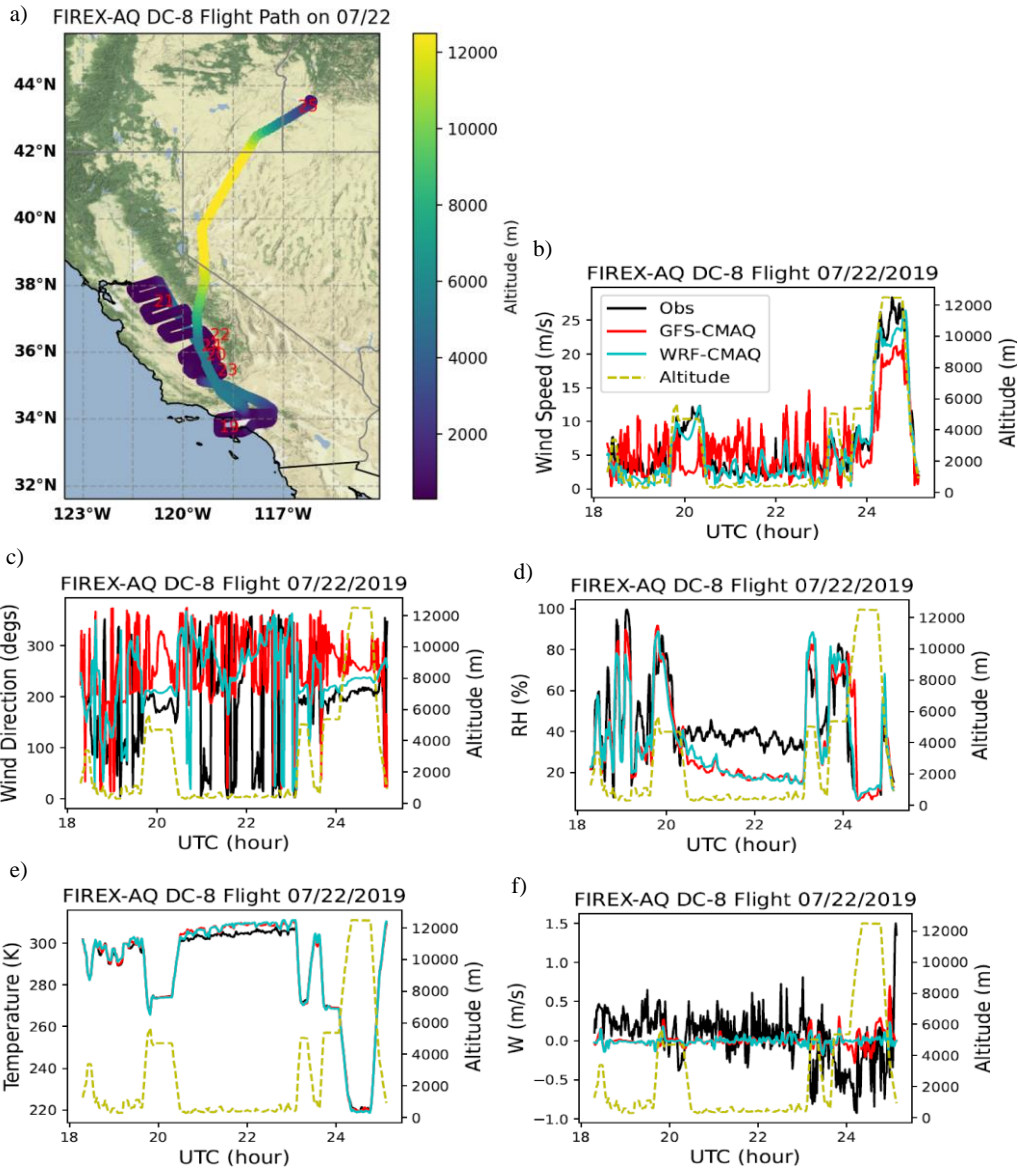
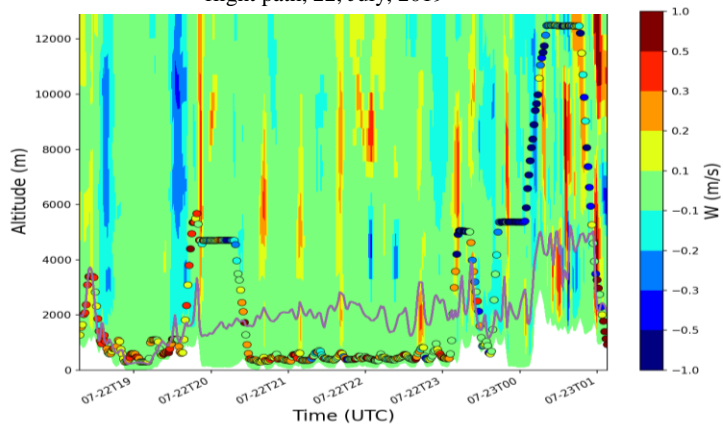


Figure 7. Modeled meteorological variables compared with observations for the DC-8 flight on 22 July, 2019 (b to f). The plot a shows the flight path colored in altitudes above sea level with UTC time in red text. Base map credits: © OpenStreetMap contributors 2022. Distributed under the Open Data Commons Open Database License (ODbL) v1.0.

a) GFS-CMAQ predicted vertical velocity along the DC-8 flight path, 22, July, 2019



b) WRF-CMAQ predicted vertical velocity along the DC-8 flight path, 22, July, 2019

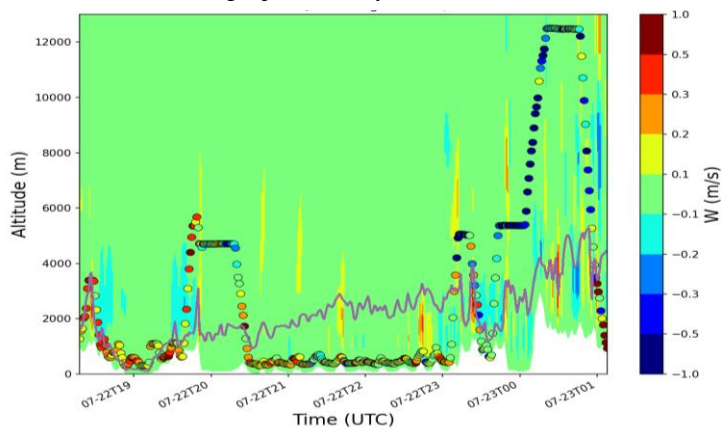


Figure 8, Curtain plots of the vertical velocity (W) predicted by GFS-CMAQ (a) and WRF-CMAQ (b) along the DC-8 flight on 22 July, 2019. The colored dots showed the DC-8 measured vertical velocities. The solid lines showed the predicted PBL heights of these two models.

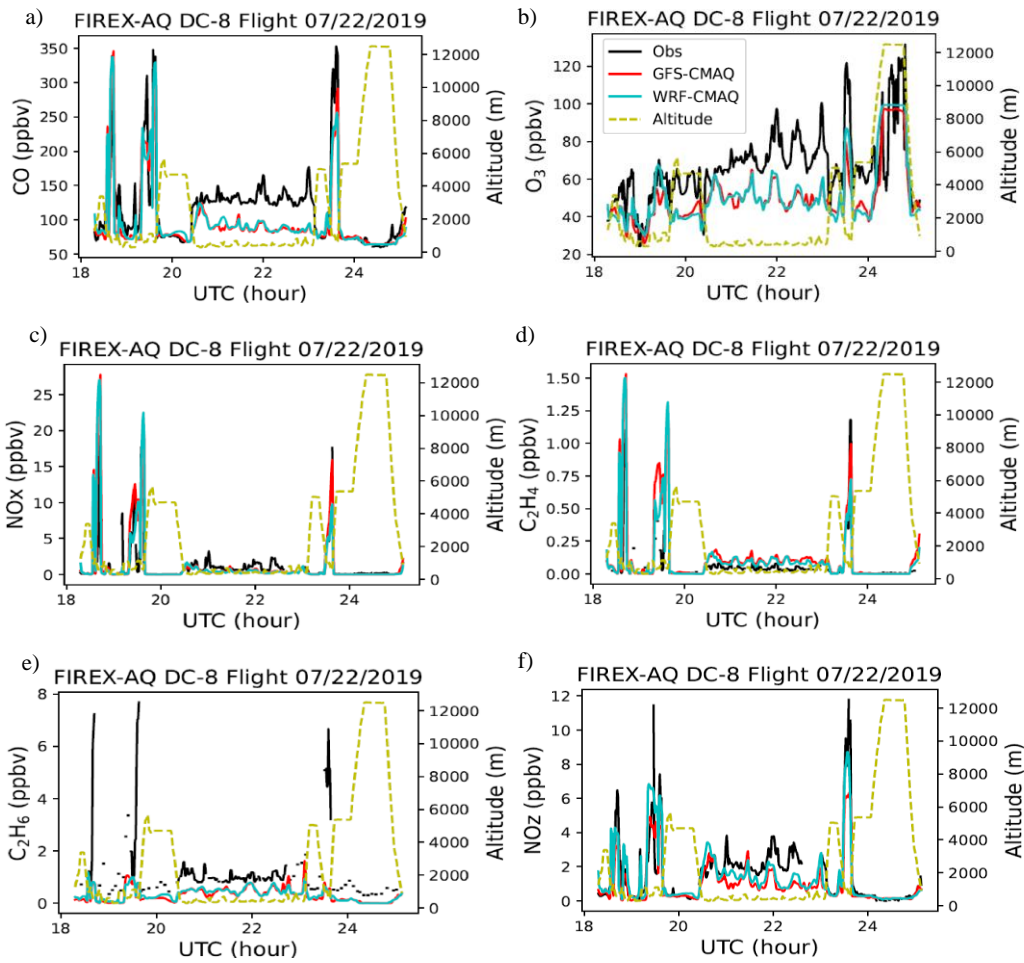


Figure 9. Model predicted chemical concentrations compared with observations along with the DC-8 flight on 22 July, 2019

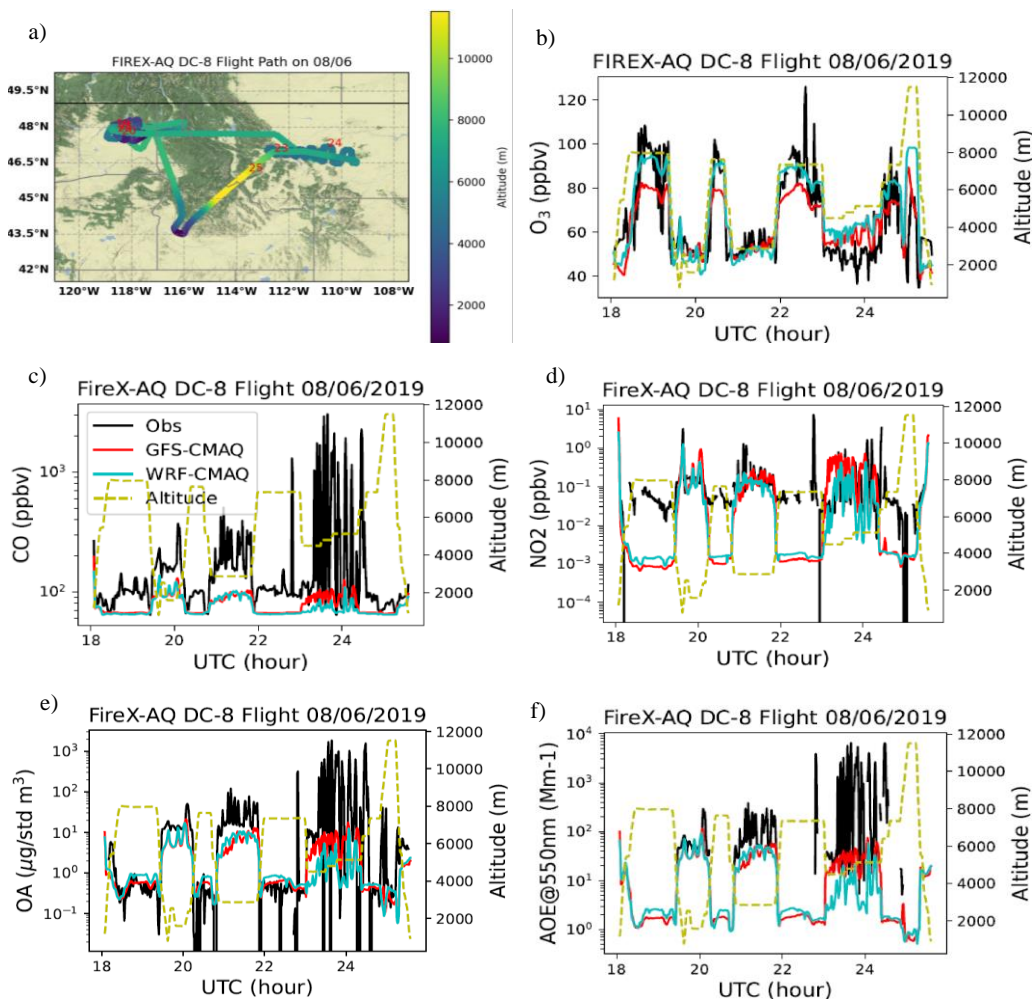


Figure 10. The DC-8 flight path (a), and model-observation comparisons for O_3 (b), CO (c), NO_2 (d), submicron organic aerosol (OA) (e) and aerosol optical extinction coefficient (AOE) at wavelength of 550nm (f) on 06 August, 2019. Base map credits: © OpenStreetMap contributors 2022. Distributed under the Open Data Commons Open Database License (ODbL) v1.0.

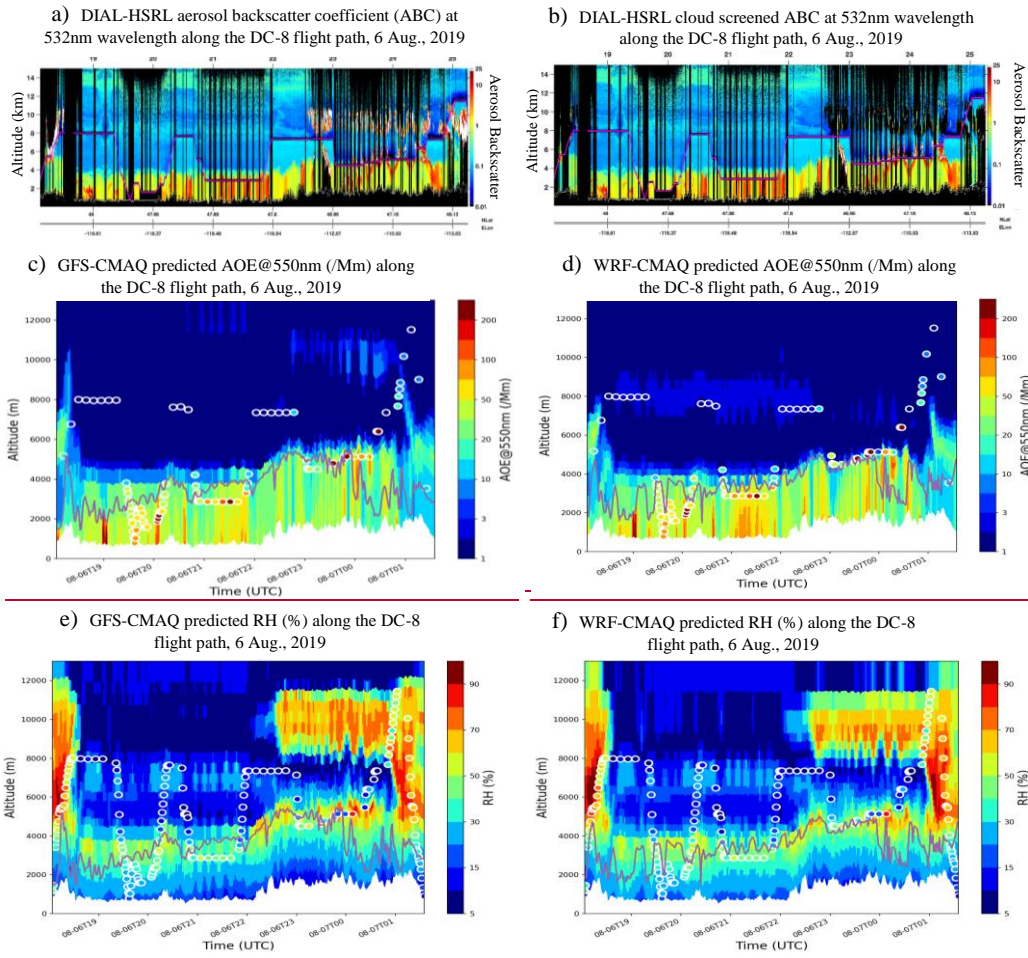


Figure 11, The Differential Absorption High Spectral Resolution Lidar (DIAL-HSRL) retrieved aerosol backscatter coefficient (ABC) at 532nm wavelength in unit /km/steradian (a) and cloud screened one (b); curtain plots of the AOE (b, c) and relative humidity (RH) (d, e) predicted by GFS-CMAQ (left) and WRF-CMAQ (right) along the DC-8 flight on 06 August, 2019. The colored dots showed the corresponding measured values. The solid lines showed the predicted PBL heights of these two models.

Supplemental Figures

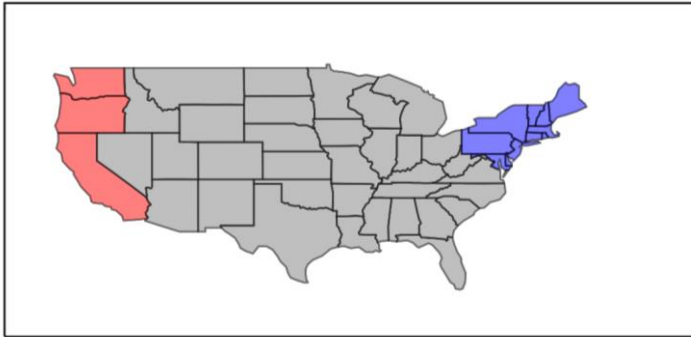
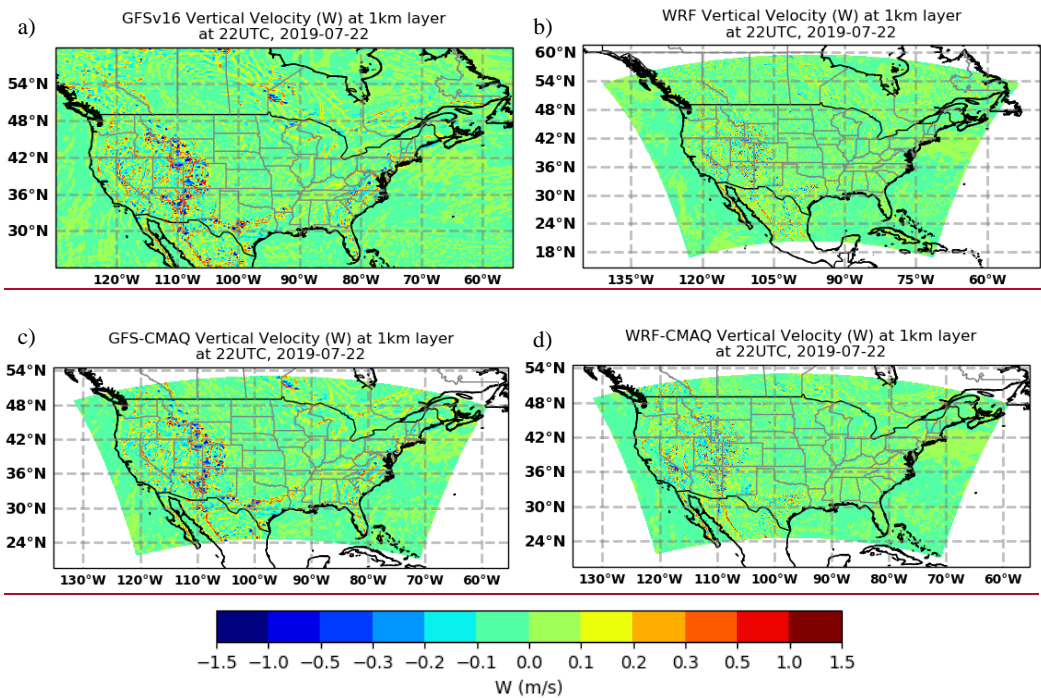


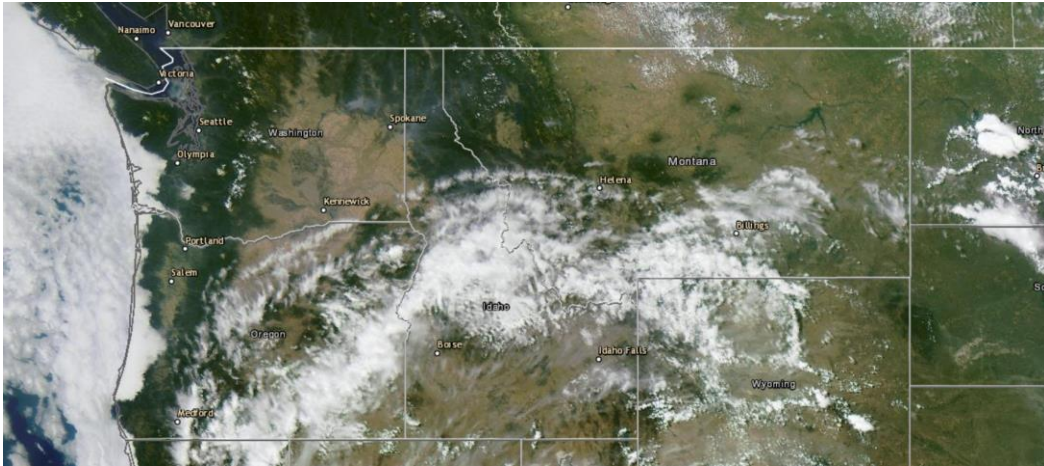
Figure S1, U.S. West (red) and Northeast (Blue) regions.



Formatted: Centered

Figure S2. The original vertical velocities of GFS (a) and WRF (b) compared to the CMAQ diagnosed W in GFS-CMAQ (c) and WRF-CMAQ (d)

a)



b)

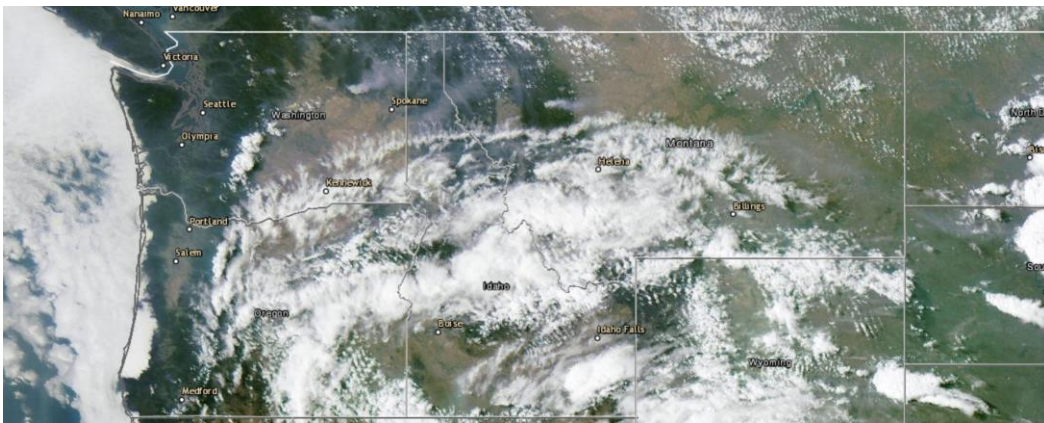


Figure S2S3, GOES-16 true color image (NOAA Aerosol Watch) at 19:41UTC (a), and 23:01UTC (b), 06 August, 2019

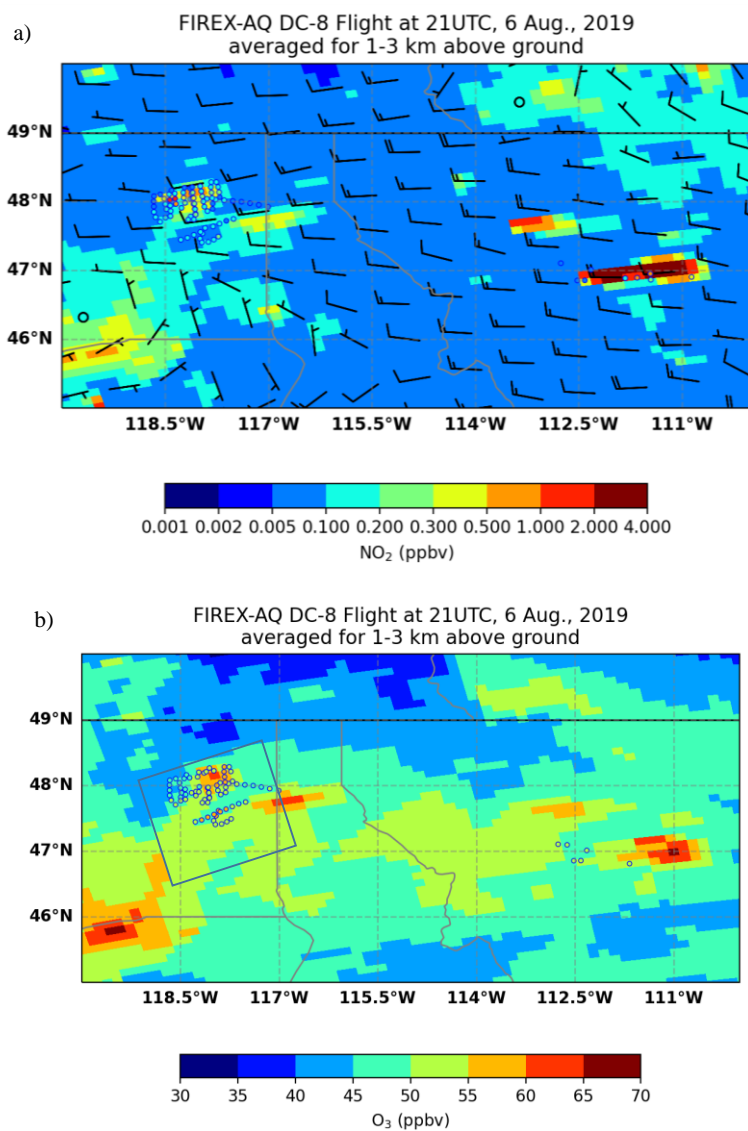


Figure S3S4. GFS-CMAQ vertical averaged NO₂ (a) and O₃ (b) for 1-3 km above ground at 21UTC compared to the DC-8 observations on 6 Aug., 2019. The plot a also shows the corresponding GFS wind field.